



**Michigan  
Technological  
University**

Michigan Technological University  
**Digital Commons @ Michigan Tech**

---

Dissertations, Master's Theses and Master's Reports

---

2023

## **AN INVESTIGATION OF MICROSEISMICITY DURING THE 2018 KILAUEA CALDERA COLLAPSE**

Isabella S. Metts

*Michigan Technological University, imetts@mtu.edu*

Copyright 2023 Isabella S. Metts

---

### **Recommended Citation**

Metts, Isabella S., "AN INVESTIGATION OF MICROSEISMICITY DURING THE 2018 KILAUEA CALDERA COLLAPSE", Open Access Master's Thesis, Michigan Technological University, 2023.  
<https://doi.org/10.37099/mtu.dc.etr/1659>

Follow this and additional works at: <https://digitalcommons.mtu.edu/etr>



Part of the [Volcanology Commons](#)

AN INVESTIGATION OF MICROSEISMICITY DURING THE 2018 KILAUEA  
CALDERA COLLAPSE

By

Isabella S. Metts

A THESIS

Submitted in partial fulfillment of the requirements for the degree of

MASTER OF SCIENCE

In Geophysics

MICHIGAN TECHNOLOGICAL UNIVERSITY

2023

©2023 Isabella S. Metts

This thesis has been approved in partial fulfillment of the requirements for the Degree of MASTER OF SCIENCE in Geophysics.

Department of Geological and Mining Engineering and Sciences

Thesis Advisor: *Gregory P. Waite*

Committee Member: *Luke Bowman*

Committee Member: *Simon Carn*

Department Chair: *Aleksey Smirnov*

# Table of Contents

Acknowledgments.....	iv
Abstract.....	v
1 Introduction.....	1
2 Background.....	3
2.1 Geology of Kīlauea Volcano.....	3
2.1.1 Fault Systems.....	3
2.1.2 Magma Reservoir.....	5
2.1.3 Hydrothermal System.....	6
2.1.4 Caldera Structure.....	7
2.2 Eruption History.....	8
2.3 Seismicity.....	9
3 Methodology.....	11
3.1 REDPy.....	11
3.2 Picking P-Wave Arrivals.....	13
3.3 Earthquake Location.....	14
3.4 Focal Mechanisms.....	16
3.4.1 HASH.....	16
4 Data.....	19
4.1 Repeating Events.....	19
4.2 Mean Frequency Index.....	22
4.3 Focal Mechanisms.....	26
5 Conclusions.....	29
6 Reference List.....	31
A Appendix.....	35
A.1 Event Waveforms for Cluster 1277.....	35
A.2 Focal Mechanisms for Viable Clusters of Interest.....	38
A.3 Interactive Picking Plots for “Crack Closing” Clusters.....	43

## **Acknowledgments**

First and foremost, I would like to thank my advisor, Greg Waite, for his patience and kindness as I navigated this project through the ups and downs of life and graduate school. Greg has always encouraged and empowered me in my education, spending hours problem-solving with me and ensuring that I understood various concepts. Despite the many times I had to postpone the end of this project, he was always ready to work with me and to help me succeed. I am grateful for his mentorship.

For sharing data to help support this project, I would like to thank Jefferson Chang with the Hawaiian Volcano Observatory. I would also like to thank Kyle Brill and Cristhian Salas Pazmiño for sharing several MATLAB and Python scripts that aided in the analysis of our data.

For impacting my decision to attend Michigan Tech and setting multiple opportunities into motion for me during my time here, I would like to thank Luke Bowman.

I would also like to thank my friends and family for their continual support and encouragement throughout this journey to further my education.

Lastly, I would like to thank my wife, who has been my number one supporter throughout graduate school and without whom I could not have done any of this.

## Abstract

The 2018 Kīlauea volcano eruption and incremental caldera collapse was accompanied by more than 60,000 seismic events cataloged by the Hawaiian Volcano Observatory as well as 62 caldera collapse events that occurred roughly once per day. The majority of seismicity occurred on the eastern side of the caldera between daily collapses. However, the majority of caldera subsidence occurred to the west. To understand the collapse mechanics behind this variance in subsidence and seismicity across the caldera region, repetitive waveforms and source properties can be studied.

Repeating seismic events suggest a common source that is not moving or destroyed. At Kīlauea, clusters of repeating events can indicate source processes throughout collapse cycles. REDPy, a repeating earthquake detector tool for Python, cross correlates seismic events to determine repetition. Events are separated into families or listed as orphans if no matches are found. We used data from HVO network stations surrounding Kīlauea's summit. Possible events were identified using an STA/LTA trigger algorithm with a long-time average trigger of 8 seconds, a short-time average trigger of 1 second, and a trigger on/off range of 1-2.5. A minimum correlation coefficient of 0.7 was used to group over 167,000 recognized events from April 29th to August 2nd into nearly 6,000 families. Of these families, 697 were chosen as 'clusters of interest' for including >100 events or persisting for 7 days or more. P-wave first-motions were manually picked for waveforms associated with clusters of interest, these clusters were then located using P-wave arrival times, and focal mechanisms were modeled for viable events to learn more about their source processes and relationship to collapse mechanics.

Dilatational first motions dominate our catalog and focal mechanism models have mismatched station polarities indicative of non-double-couple sources. In fact, focal spheres show evidence of reverse motion on ring faults, which is the opposite sense of slip associated with the large, daily caldera collapse events. This change in slip direction suggests that much of the microseismicity results from shortening within the down-dropped caldera and rebound in areas adjacent to the caldera.

# 1 Introduction

Caldera collapse mechanics prove difficult to study in real time due to their rarity and, often, rapid development. From 1900 to 2014 only seven caldera forming events are on record, most of which occurred prior to the invention of modern-day geophysical monitoring equipment (Gudmundsson et al., 2016). The 2014 caldera collapse event at Bárðarbunga volcano in Iceland is one of the only sequences, other than the 2018 Kīlauea collapse, with the opportunity to study collapse mechanics using a variety of geophysical data in real time (Gudmundsson et al., 2016). Through studying collapse sequences at Bárðarbunga volcano, Gudmundsson et al (2016) describes the relationship between eruption and collapse mechanisms as heavily intertwined, driving one another throughout the sequence once an initial collapse is triggered.

Magma chamber decompression, a result of magma drainage during eruption, is the more accepted model for triggering collapse in caldera forming volcanoes (Acocella, 2007). Five end-member collapse types describe surface depression and faulting at collapse sites: downsag, trapdoor, funnel, piecemeal, and piston style structures (Acocella, 2007). Calderas in hot spot and rift zone regions tend to have visible piston style structures, though studies have revealed that other end-member styles often overlie evidence of a piston collapse system (Acocella, 2007). Evidence of piston style collapse beneath various end-members indicates a more complex, multi-phase, process behind collapse mechanisms.

The 2018 eruption sequence and cumulative caldera collapse at Kīlauea Volcano in Hawaii produced some of the most coherent collapse data to date through continuous monitoring by the Hawaiian Volcano Observatory (HVO) and their extensive seismic network. The present caldera structure at Kīlauea was rapidly altered during the 2018 eruption sequence as a result of 62 cyclical caldera collapse events between May and August. Each collapse event produced a  $M_w$  5.2 - 5.4 earthquake (Shelly & Thelen, 2019) with microseismicity dominating inter-collapse sequences. As collapse events began to occur cyclically, nearby monitoring equipment was able to capture repeated evidence of inter-collapse seismicity and patterns leading up to collapse that had not previously been recorded for any other caldera producing volcano. The amount of data available for the 2018 eruption sequence has changed how caldera collapse mechanics can be studied.

Cumulative collapse during the 2018 eruption caused the Halema'uma'u Crater's diameter to increase by more than 1500 m and subside by 500 m (Shelly and Thelen, 2019). Previous analysis of seismicity occurring throughout the eruption indicated that the majority of events cataloged by HVO occurred to the east of the Halema'uma'u crater, while the majority of subsidence occurred on the western side of the crater (Shelly & Thelen, 2019). Sources behind the various types of seismicity occurring throughout the eruption can inform about their relationship to collapse mechanics and explain discrepancies between seismically active regions and regions of maximum subsidence.

In order to study cyclical collapse mechanics, we focused on source mechanisms of repeating microseismic events throughout the eruption sequence. Repeating events are representative of dominant processes and the presence of multiple events allows for a more accurate source interpretation through waveform stacking. Repetition through this eruption sequence is indicative of a source that is not destroyed by various collapse events. As seismicity continues to repeat throughout the eruption sequence it becomes

increasingly more likely that the unchanged triggered source is aiding collapse mechanics. In this study, we analyzed repeating clusters of interest based on longevity and event quantity to limit our data to events that may relate to collapse mechanisms. We performed waveform analysis, hypocenter relocation, and produced focal mechanisms for our clusters of interest to improve comprehension of source mechanisms and spatial relationships between events and local volcanic systems.



## 2 Background

Kīlauea volcano, located on the southeast flank of Mauna Loa Volcano on the island of Hawaii, is a tholeiitic shield volcano accompanied by two major rift zones. Formed by intraplate hotspot volcanism, Kīlauea is a result of the Pacific Plate moving southeast across a mantle plume (Calvert & Lanphere, 2006). Due to frequent effusive eruptions, Kīlauea is considered to be the most active volcano in the world with 90% of its surface rock being less than 1,100 years old (Lipman et al., 2002). Structural features include Kīlauea’s summit caldera, the East Rift Zone (ERZ), and the South West Rift Zone (SWRZ) (Fig. 1). In addition to the caldera and rift zones, Kīlauea contains two major fault systems, the Koa’e Fault System and the Hilina Fault System (Podolsky & Roberts, 2008).

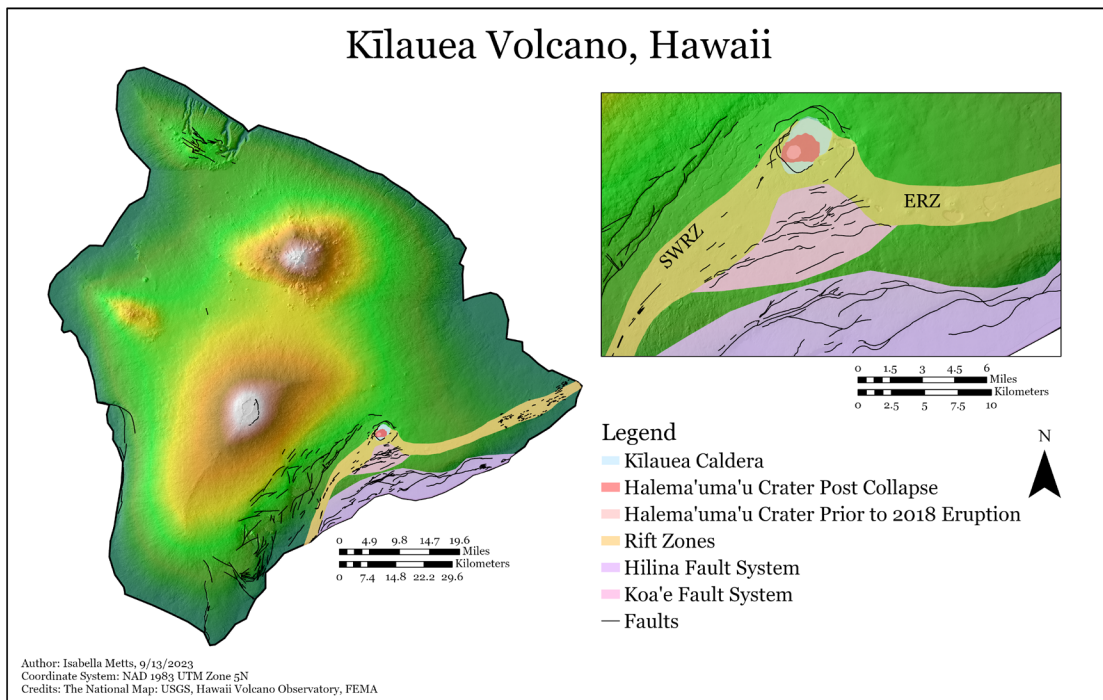


Figure 1. A map of volcanic structures and fault systems at Kīlauea Volcano, Hawaii.

### 2.1 Geology of Kīlauea Volcano

#### 2.1.1 Fault Systems

The Koa’e Fault System is an area of normal faulting south of Kīlauea’s caldera that trends in an east/north-east direction. The Koa’e Fault System stretches from the South West Rift Zone to the East Rift Zone, covering a zone of around 12 km in length and between 1 km and 3 km in width, disconnecting the southern flank of the volcano from the rest of the structure (Podolsky & Roberts, 2008). A basal detachment fault at the base of Kīlauea’s edifice, located between a depth of 8 and 10 km, carries the south flank WSW towards the sea at a maximum rate of 10 cm/year (Wang et al., 2019). In addition to creep along the basal detachment fault, dilation of the rift zones from steeply dipping

dikes pushes the south flank of the volcano further south, growing this fault system with each intrusion (Duffield, 1975).

Structures within the Koa'e fault system consist primarily of northern facing fault scarps, relay ramps resulting from an en-echelon style of faulting, and occasional monoclines. It has been suggested that the Koa'e Fault System originally formed as a result of footwall uplift associated with deformation along the Hilina Fault System, located towards the base of Kīlauea's south flank. The northern facing fault scarps, common throughout the Koa'e Fault System, do not correlate with the fault system's seaward direction of extension and footwall uplift models account for this discrepancy (Parfitt & Peacock, 2000). Though footwall uplift is a likely explanation for the fault system's origin, current deformation throughout the fault system is heavily associated with magmatism and fault movement at depth.

Magmatism throughout the bounding rift zones induces stress and pressure that extends into the Koa'e Fault System, producing surface level cracks and triggering slip along faults. As stress from a single rupturing fault at depth propagates upward, en-echelon style fractures of similar stepping direction emerge at the surface. These en-echelon style cracks are often seen along the surface of relay ramps, indicating movement related to the bounding faults of the ramp. Relay ramps form as zones of ground deformational tilt between en-echelon normal faults with identical dipping directions and are often the result of the fault segments connecting at depth. Deposition of overlying volcanics between fault motions causes growth faulting within the Koa'e Fault System and upward fault propagation beneath younger solidified lava flows has produced monoclinic structures along the surface (Podolsky & Roberts, 2008).

The Kulanaokuaiki Pali, the southernmost fault scarp of the Koa'e Fault System, is thought to connect to a single underlying fault extending 15 km in length and striking ENE (Ge et al., 2019). It is possible that the fault underlying the Kulanaokuaiki Pali extends to the base of the edifice and connects to the basal fault. At least one other underlying fault is present within the fault system, possibly more (Parfitt & Peacock, 2000).

Also located on the south flank of Kīlauea is the Hilina Fault System, another zone of normal faulting below the Koa'e Fault System. The Hilina Fault System marks a structural and seismic boundary along the south flank, distinguishing this portion of the flank from the Koa'e fault system through contrasting deformational patterns (Lipman et al., 1985). Within the Hilina Fault System southern facing fault scarps up to 500 meters in height and relay ramps between interacting fault segments are found (Parfitt & Peacock, 2000). En-echelon style faults varying in length, but often ranging around hundreds of meters, dominate the fault system. The amount of displacement indicated by the size of the fault scarps is inconsistent with the faults surface length and suggests a connection between the Hilina Fault System and the basal fault (Parfitt & Peacock, 2000). The use of seismic tomography has solidified this claim that the Hilina Fault System connects to the basal fault by proving that the fault system extends to depths between 9 km and 11 km, while the basal fault resides around 9km. Seismic tomography has also demonstrated that the Hilina Fault System is a structural boundary between land materials of higher velocities and materials of lower velocities towards the sea,

reinforcing claims grounded in seismic and deformational trends (Parfitt & Peacock, 2000).

The origin of the Hilina Fault System is presumably associated with the movement along the basal fault. It has been suggested that a variance in slip rate between the portions of the basal fault north and south of the Hilina Fault System played a role in the systems development (Parfitt & Peacock, 2000). One fault is thought to underlie the entire system, stretching around 42 km in length and extending to the base of the edifice to connect with the basal fault (Parfitt & Peacock, 2000).

The entirety of Kīlauea's south flank is considered to be a part of a slow-moving landslide, with both the Hilina and Koa'e Fault Systems contributing to the movement of this structural block towards the Pacific Ocean. The two fault systems show distinctly different deformational and seismic patterns, but both contain evidence of a connection with larger faults at depth. The Hilina Fault System connects to the basal detachment fault through an underlying fault segment and it is likely that the Koa'e Fault System has ties to the basal fault as well. These two fault systems are heavily connected, with the origin of the Koa'e Fault System having ties to secondary deformational patterns associated with large-scale normal faulting in the Hilina Fault System. Deformational studies of Kīlauea are not complete without consideration of these fault systems and their impact on the entirety of the volcano.

## **2.1.2 Magma Reservoir**

A deep-seated mantle plume drives Kīlauea's eruptions. Interactions between the mantle plume and the south-eastward moving Pacific Plate induce melting of upper-mantle and lithosphere, providing a source of magma to the volcano. Magma rises through a nexus of sills connected through short vertical conduits between depths of 7 km and 40 km (Wilding et al., 2022), and is stored in an overlying reservoir, between 2 km and 7 km, that houses a network of smaller conduits, cavities, and pathways (Almendros et al., 2001). The location of maximum subsidence within a caldera system, the Halema'uma'u Crater within the Kīlauea Caldera, directly overlies this magma reservoir (Kauahikaua, 1993). Kīlauea's two rift zones connect to the reservoir temporarily storing magma through horizontal pathways that allow for the transfer of magma down rift. As magma pressurizes in these conduits, cavities, and pathways the overlying crust can crack and initiate eruption.

Prior to eruption, ground deformation can be a strong indicator of magma traveling through the subsurface. As magma travels up from the mantle and is stored in overlying chambers, pressure begins to increase and the surface swells (Kauahikaua, 1993). Inflation and deflation related to ground motion in volcanic regions can be precursors to eruptive and seismic events. Earthquakes occur when the pressure within a magma chamber exceeds the strength of the surrounding material, leading to the deformation of rock in both the surface and subsurface. The location of these earthquakes can provide insight on the location of magma chambers as well as the direction of magma travel through conduits and pathways.

### 2.1.3 Hydrothermal System

Kīlauea's shallow hydrothermal system is driven by the heat from crustal magma storage. Groundwater present at Kīlauea is subject to heat transfer from nearby melt leading to a pressure increase in fluid filled cracks, production of bubbles and steam, and often triggering the rapid discharge of fluids, producing distinct seismic signatures (Kumagai et al., 2004).

The rich history of geophysical studies of Kīlauea's hydrothermal system include gravity, seismic-velocity, and electrical resistivity to determine location and depth of groundwater. The uniformity of Kīlauea's lithology implies that any variation in recorded densities should be attributed to water saturation or basalt vesicularity. Bouguer anomaly values for the island of Hawaii show sizable anomalies to the south of the summits of each of the five volcanoes located on the island (Kauahikaua, 1993). Focusing on Kīlauea, a positive gravity anomaly is located within the caldera and gravity ridges are present along the two rift zones. Gravity ridges associated with the upper east rift zone and the southwest rift zone are slightly displaced to the north and may be indicative of early rift locations. These gravitational anomalies of around 300 mGals have been attributed to the presence of dense dikes rather than water saturation. Seismic-velocity distributions produced similar results to the gravitational anomaly mapping, showing that the Kīlauea caldera and associated rift zones overlie rocks with abnormally high P-wave velocities when compared to surrounding velocities (Kauahikaua, 1993). Resistivity studies aid in further understanding the saturation levels of the subsurface structure depicted by gravitational and seismic studies, as dry basalts have extremely high resistivity values when compared to saturated basalts (Kauahikaua, 1993). Studies measuring subsurface resistivity up to 1km beneath Kīlauea's summit found resistivities upwards of 3000 ohm m at Kīlauea's surface overlying resistivities spanning from several hundred to less than 30 ohm m (Kauahikaua, 1993). Groundwater saturation in basalts can be distinguished into fresh water and salt water saturation using these resistivity values, with resistivities between 100 and 600 ohm m indicating fresh water presence and resistivities less than 30 ohm m indicating salt water presence. A 1209 m deep drill hole within the caldera boundary confirmed water table presence more than 600 meters above sea level where salinity levels matched that of a low resistivity fluid and a maximum temperature of 137 C was recorded. Resistivities measured between the summit and the Koa'e Fault Zone, a triangular region bounded by the fault system and the northern edges of each rift zone, present a low resistivity zone that is not present outside of these bounds (Kauahikaua, 1993). Hydrothermal systems commonly contain fluids with high saline contents due to chemical interactions with surrounding rock and magma (Nehlig, 1991). Conflicting models depicting resistivity beneath 1 km have been presented, but do not aid in quantifying the extent of Kīlauea's hydrothermal system beyond this low resistivity zone.

More recent studies of Kīlauea's hydrothermal system study sources linked to long-period (LP) seismic events and tremor. In order to determine the spatial extent of Kīlauea's hydrothermal system LP events and tremor can be utilized due to their common source involving fluid-crack interactions. A study analyzing 1129 LP events that occurred in a February 1997 swarm has shown that LP events often originate northeast of the Halema'uma'u Crater in a location of intense fracture, where multiple eruptions have

been recorded, and a known magma conduit has been mapped (Almendros et al., 2001). Of the 1129 LP events studied, 857 hypocenters were located in this northeastern region at depths of 200 m or less, indicating that a significantly active portion of the near-surface hydrothermal system is confined to this area of the caldera. Of the other 272 events studied, 131 hypocenters were located at depths of 200 m or less southeast of the Halema'uma'u Crater, 132 hypocenters were located beneath the Halema'uma'u Crater at depths closer to 400 m, and 9 were located outside of these specified regions (Almendros et al., 2001). This study also analyzed 147 tremor events and found 146 of them to have originated in the same northeast source region where the majority of LP events occurred. The shared source region for LP events and tremor, both considered a form of LP seismicity, is consistent with their analogous source mechanisms rooted in fluid dynamics and differentiated by the duration of acoustic resonance.

The source region northeast of the Halema'uma'u crater overlying a known magma chamber suggests that any groundwater present would be subject to hydrothermal processes. The resulting seismic signals could arise from a multitude of interactions between the hydrothermal system and underlying magma including degassing, boiling groundwater, steam production, pressure variations, and induced fluid travel.

#### **2.1.4 Caldera Structure**

The current summit caldera at Kīlauea Volcano has formed through a complicated series of eruption sequences ultimately draining underlying magma chambers and enabling the collapse of surrounding rock. Lava flows present prior to the formation of the current caldera and tephra from post-caldera eruptions have been dated using <sup>14</sup>C methods to place caldera formation between 1470 and 1510 CE (Zurek & Williams-Jones, 2013). Cycles of caldera collapse and fill continually alter the structure with emerging lava raising the caldera floor and eruptive events leading to its inevitable collapse. It is hypothesized that an ancient caldera structure was present prior to 1500 CE, but due to persistent effusive eruptions older structures are not visible at the surface (Zurek & Williams-Jones, 2013). Gravity mapping techniques used to investigate the hydrothermal system have also been used to investigate the shallow subsurface at Kīlauea's summit in an attempt to understand the magma plumbing system and near-surface caldera structure. While a Bouguer anomaly study could identify dense material beneath the summit and rift zones at Kīlauea, dynamic gravity surveys were needed to provide additional detail on that shallow subsurface. Multiple dynamic gravity surveys have been conducted in the past 50 years in order to detect change in shallow subsurface gravitational fields in relation to large earthquakes and eruptions. These dynamic gravity surveys can detect an increase or decrease in mass below the surface, providing insight into magma drainage and migration over time. The volume of void or filled space can also be determined through these surveys. Through dynamic gravity surveying a 1975 M7.2 earthquake was associated with the formation of a 40-90 x 10<sup>6</sup>m<sup>3</sup> empty reservoir underlying the summit center, northeast of the Halema'uma'u Crater, as a result of crack production and magma drainage (Zurek & Williams-Jones, 2013). This void space has since shown signs of fill, with dynamic gravity surveys taken in 2008 measuring an increase in the local gravitational field. After correcting for 1.9m of subsidence during

this time period, the increase correlated with  $21-120 \times 10^6 \text{ m}^3$  of fill associated with vertical migration of magma into the chamber and the crystallization of olivine cumulates out of present magma (Zurek & Williams-Jones, 2013). This is one example of how the subsurface in volcanic regions is subject to constant alteration. In conjunction with the filling of a void space, rifting at the summit can account for a percentage of the increase seen in later dynamic gravity surveys, as well as provide a method for olivine cumulate formation. North-south rifting, implied by the northeast-striking fissures and underlying magma pathways, as a method of magma reservoir expansion provides the needed conditions for enough olivine cumulate to form to be present after a collapse event (Zurek & Williams-Jones, 2013). The high-density gravity anomaly present beneath the center of the caldera has been presumed to be a remnant of a drained magma reservoir, likely consisting of this olivine cumulate, present before the formation of Kīlauea's current caldera (Zurek & Williams-Jones, 2013). The growth patterns behind these magma reservoirs provide insight on the behavior of the magma plumbing system at Kīlauea, as well as into possibilities of cyclical caldera formation.

Conceptual models describing caldera collapse classify collapse mechanisms into five geometrical categories: piston, downsag, trapdoor, piecemeal, and funnel (Acocella, 2007). These models act as end members with true collapse mechanisms falling somewhere in between the geometries listed. Piston-style models consist of a single structural block surrounded by a ring fault, presenting more of a true crater in the earth's crust. Downsag models depict the crust sagging, usually in the form of a large inwardly dipping depression. Trapdoor models also show an inwardly dipping depression, but in an asymmetrical form where one side has the majority of subsidence. Piecemeal models describe the varied subsidence of multiple structural blocks within an area of collapse and funnel models depict a cone shaped indentation, often with more depth than width. Kīlauea's caldera is often compared to the piston model as areas of collapse subside within ring fault bounds.

Shelly and Thelen (2019) characterize the mechanisms behind collapse at Kīlauea's caldera into four stages. Stage 1 begins with magma drainage that results in a pressure decrease, causing dikes to close (stage 2) and faults to slip (stage 3), ultimately leading to the subsidence of a piston-style structural block in stage 4. The piston-style collapse repressurizes the system and restarts the cycle (Shelly & Thelen, 2019).

## **2.2 Eruption History**

Due to predominantly young surface material at Kīlauea, the eruptive history that is best understood by scientists is limited to the past 2500 years. At Kīlauea's summit, continuous eruption, often lasting years at a time, characterizes the volcanic activity of this zone. Prior to the formation of Kīlauea's current caldera, the formation of an ancient caldera structure 2200 years ago marked a drastic change from effusive eruptions to explosive eruptions. Swanson et al. (2014) describes Kīlauea's eruptive history through explosive and effusive periods. Ash deposits and lava flows have been studied to determine the approximate timing of explosive periods, interrupting Kīlauea's more common periods of effusion. The Uwēkahuna Ash and the Keanakāko'i Tephra Member are stratigraphic examples of explosive deposits at Kīlauea. The Uwēkahuna Ash was

found to contain evidence of explosive eruptions for a 1200 year period from 200 BCE to 1000 CE. Throughout this explosive period, little evidence of effusion is found. Only three lava flows are found throughout the Uwēkahuna Ash, a significantly small number for a primarily effusive volcano. The following explosive period is marked by the Keanakākoʻi Tephra Member with deposits dating back to 1500 CE. This explosive period was found to last around 300 years, with evidence of only one lava flow, ending in 1800 CE. Effusive eruptions resumed, leading to the construction of the Observatory shield after the present caldera had been filled. The effusive ‘Ailā‘au lava flow erupted out of the eastern side of the shield until 1470 when the current Kīlauea caldera was formed through collapse of the Observatory shield, resulting in 600 m of subsidence across a depression with diameters of 3.5 and 3 km. With the formation of the Kīlauea caldera came another duration of explosive eruptions, lasting until the early 1800’s when effusive eruptions returned. Outside of the explosive periods associated with caldera formation, Kīlauea has been mainly effusive. This pattern of effusive to explosive periods suggests that there may be a cycle within Kīlauea’s eruptive sequences (Swanson et al. 2014).

For a century, between 1823 and 1924, Kīlauea was in a period of summit unrest accompanied by multiple instances of caldera collapse and shield formation. In February, 1924 magma drainage from the Halema‘uma‘u lava lake and subsequent seismic swarms along the lower east rift zone foreshadow an explosive eruption occurring in May, 1924. April was filled with an increase in seismicity, likely associated with magma transportation, and ended with collapse of the crater floor. For nearly three weeks in May, 50 explosive events characterized the eruption sequence. The explosive quality of these events was likely a result of activity in Kīlauea’s hydrothermal system where groundwater interactions with recently emptied magma conduits produces steam, increases pressure in the conduit, and results in the explosion of debris.

After the 1924 eruption, and prior to the 2018 eruption, summit eruptions were not common at Kīlauea. From 1983 to 2018 Kīlauea had been erupting from the eastern rift zone, specifically near the Pu‘u ‘Ō‘ō eruption vent (Holcomb, 1987). On April 30th, 2018 the Pu‘u ‘Ō‘ō eruption vent, located in the eastern rift zone of Kīlauea volcano, collapsed and began to allow magma movement down the rift. This collapse launched an eruption sequence that lasted into September. Two days post-collapse the lava lake within the Halema‘uma‘u crater at Kīlauea’s summit began to see a drop in volume, with lake levels reaching 325 meters beneath the crater floor by May 10th. Fissures began to open within the lower east rift zone with lava flow becoming hotter and faster as eruptive lava transitioned from an older magma stored in the rift zone to that draining from the lava lake. May 16th marked the first of many summit collapses and by May 29th collapse events at the summit were occurring almost daily. By early August 62 collapse events had occurred within the Halema‘uma‘u crater. The combined subsidence from all collapse events left the Halema‘uma‘u crater 500 m deeper and 1500 m wider than measurements recorded prior to the eruption sequence.

## **2.3 Seismicity**

On July 31st, 1912 the Hawaiian Volcano Observatory deployed the first seismographs in the observatory, initiating over a century of geophysical monitoring. The

original seismographs installed in Hawaii came from Fusakichi Omori, an innovator in the world of volcano seismology who designed equipment capable of recording local and distant seismicity. The two seismographs obtained by HVO were distinguished by the “ordinary” and “heavy” weights used in their construction, with the heavy seismograph being more sensitive to weak motions and commonly recording ocean microseisms (Okubo et al., 2014). HVO later began designing seismic instruments, aiming towards a compact device with improved sensitivity, and distributing them across the island of Hawaii. The field of volcano seismology advanced through work done at HVO; earthquake monitoring evolved into studies of seismic behavior and volcanic source processes. Today the HVO network on the island of Hawaii consists of more than 60 seismic instruments, most of which have transitioned to broadband seismometers that are capable of recording an extensive range of seismic signals.

Seismicity in volcanic regions can inform scientists of subsurface activity, specifically related to eruption mechanics, improving hazards predictions and our understanding of near-surface geophysics. Volcanic seismicity is often categorized into three groups based on source processes that impact signal duration, frequency range, and waveform characteristics. Very long period (VLP) seismicity refers to seismic signals consisting of extremely low frequencies, 0.01 to 0.5 Hz, that record fluid transport such as magma traveling through a conduit (Chouet & Matoza, 2013). Long period (LP) seismicity accounts for long period signals as well as tremor, both of which produce frequencies between 0.5 and 5 Hz. Chouet and Matoza (2013) describe long period signals as being characterized by a “brief broadband onset, followed by a coda of decaying harmonic oscillations”, indicating a trigger mechanism and subsequent fluid-filled resonator response. Tremor tends to produce long duration signals with less clear onsets than long period events, recording acoustic resonance without the distinctive trigger (Chouet & Matoza, 2013). Volcano Tectonic (VT) seismicity refers to higher frequency signals, between 5 and 15 Hz, recording brittle failure, similar to earthquakes occurring in non-volcanic regions, but powered by volcano processes. P-wave arrivals for VT signals are usually impulsive and source processes tend to involve double couple mechanisms. Crack forming events, referred to as tensile failure, can also produce VT signals, resulting in non-double couple mechanisms. A fourth category is often used to describe events that fall between LP and VT descriptions. Hybrid signals have similar waveform characteristics to LP seismicity, but produce a higher range of frequencies and evidence of shear failure in the first motions. The trigger mechanism behind the harmonic oscillations, or resonance, of a hybrid event is brittle failure of some kind (Chouet and Matoza, 2013).

Waveform classification provides insight into seismic source processes and the volcanic processes occurring throughout eruption sequences. Repeating earthquakes are individual seismic events that produce very similar waveforms, indicating that they were generated from the same source process. Repeating events can occur along faults (VTs) or in pressurized cracks (LPs). When events repeat it is indicative of a source that is not being altered over time. At Kīlauea, the constant volcanic activity and subsurface modification suggests that any source that is not moving or being destroyed may be vital to the mechanisms behind local volcanism.



## 3 Methodology

### 3.1 REDPy

We identified regions of long-lived faults and fractures that host repeated earthquakes by cross correlating a catalog of event waveforms to determine repetition. To produce a catalog of seismicity that occurred during the 2018 eruption sequence we used REDPy, a repeating earthquake detector tool for python (Hotovec-Ellis & Jefferies, 2016) to download and sort data from EarthScope’s SAGE facility (previously IRIS). When given a range of applicable dates, REDPy downloads data from user input stations, determines qualifying events using an STA/LTA trigger algorithm, then loops through and cross correlates the seismic events given a user input correlation coefficient. The events are then separated into two groups; repeating events are grouped with those that have similar waveforms as “families” (Appendix A.1) and earthquakes with no matches are considered “orphans”. The first event in a family is labeled as the “core” event and all future waveforms are cross correlated against this core. As correlations are made, the core event for a family can change based on which waveform in a family best correlates with all other members. If a waveform correlates with multiple core events, then the families are merged together. Orphans are kept in a table for cross-correlation for 7 days before they are considered “expired” and removed from the cross-correlation pool. An OPTICS (Ordering Points to Identify the Clustering Structure) algorithm is used to order the events in each family, where the distance between events is controlled by the user-defined correlation. REDPy saves a number of tables to an .h5 file that acts as a database for an individual REDPy project. The .h5 file holds trigger tables, repeater tables, orphan tables, correlation tables, deleted tables, and junk tables. REDPy also produces text files containing catalog, core event, and orphan data and provides interactive bokeh plots for the entire catalog as well as individual families. Plots for each catalog include an orphan vs. repeater plot, a frequency index plot, an occurrence timeline, and a cluster longevity plot. Individual cluster pages contain a plot depicting core and stacked waveforms on each station, a frequency plot summing the Fourier amplitude spectra on all stations, an amplitude timeline, a timeline illustrating the time between events, and a timeline of correlation-coefficient values (Fig. 2).

<Cluster 1276 | Cluster 1277 >

### Cluster 1277



Number of events: 110  
Longevity: 5.76 days  
Mean event spacing: 1.27 hours  
Median event spacing: 0.38 hours  
Mean Frequency Index: -0.26  
First event: 2018-06-11T01:55:08.015000  
Core event: 2018-06-12T07:39:58.825000  
Last event: 2018-06-16T20:07:55.175000

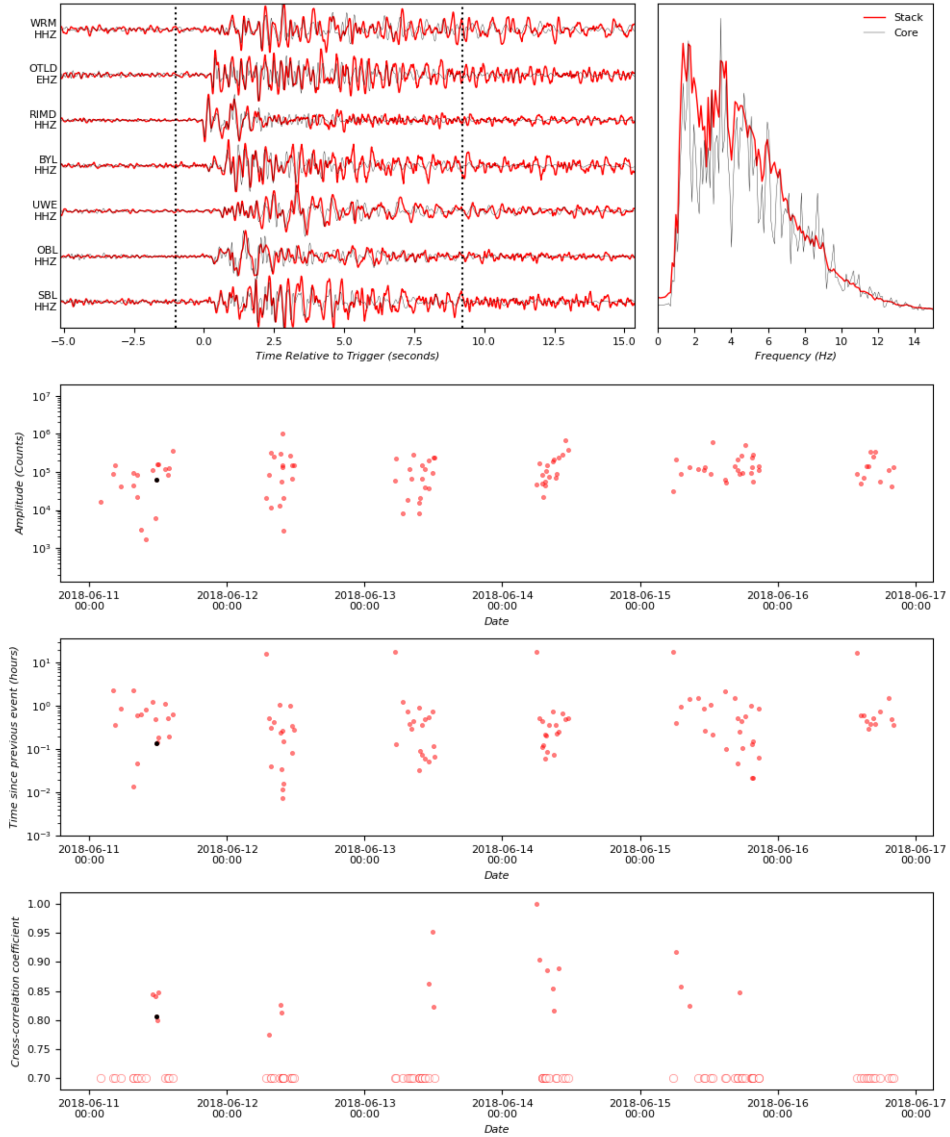


Figure 2. Individual cluster page produced by REDPy for cluster 1277.

For the 2018 Kīlauea eruption, we used data from stations SBL, OBL, WRM, OTLD, RIMD, BYL, and UWE in the HV network through the SAGE database (Fig. 3). At the time of the 2018 eruption sequence all stations used were high broadband, high gain with the vertical component of interest with the exception of OTLD, which was an extremely short period, high gain station. The seven stations chosen for data collection surround Kīlauea’s summit, providing a 360 degree view of seismic activity. Station code, network, channel, and location were input into REDPy’s setting script in order to gather data.

Possible events were identified using an STA/LTA trigger algorithm with a long-time average trigger of 8 seconds, a short-time average trigger of 1 second, and a trigger on/off range of 1-2.5. STA/LTA algorithms calculate average amplitudes over two moving windows, a long-time window and a short-time window, determining what seismicity qualifies as an event using a trigger threshold. Once the trigger threshold is breached by the ratio of short-time average to long-time average an event is cataloged. A classic STA/LTA algorithm uses a long-time average trigger of 8 seconds, a short-time average trigger of 0.7 seconds, and a trigger off/on range of 2-3. A recursive STA/LTA algorithm uses a long-time average trigger of 3 seconds, a short-time average trigger of 8 seconds, and an on/off trigger range of 1-2.5. We kept the classic STA/LTA long time average trigger and slightly raised the short-time average trigger to act as a filter for false triggers while still recording small events. We chose to decrease the trigger on/off range to 1-2.5 to increase the likelihood that smaller events will be recorded as triggers. A minimum correlation coefficient of 0.7 was used to group over 167,000 recognized events from April 29th to August 2nd into nearly 6,000 families.

Due to the abundance of seismicity occurring during this eruption sequence, we split the data into three REDPy catalogs for processing efficiency. The first catalog (C1) includes data from April 29th to June 18th, the second catalog (C2) includes data from June 18th to July 6th, and the third catalog (C3) includes data from July 6th to August 2nd. Splitting the data between files allows for an area of bias, specifically in how the events are grouped near the dates in which the files overlap.

Interactive plots produced by REDPy provide cluster data on longevity, event quantity, mean frequency index, as well as mean and median event spacing. Of the nearly 6,000 families cataloged, we determined that our clusters of interest would be families that contain 100 or more events and families that have a duration of 7 days or longer. Using this criteria, 86 families were cataloged from C1, 112 families from C2, and 499 families from C3, totaling 697 clusters of interest. Of the 697 clusters of interest, 21 clusters were filtered out for their distance from the caldera and study region, leaving 676 clusters of interest for analysis.

### **3.2 Picking P-Wave Arrivals**

Once the clusters of interest were chosen, the P-wave arrivals and first motions were picked for each station in each cluster utilizing phase weighted and linear stacks of each family. Phase weighted stacks of the waveform data were utilized for picking purposes with linear stacks acting as an additional resource when P-wave arrivals were emergent and difficult to differentiate from background data in the phase weighted stacks. A MATLAB code written by Kyle Brill (2019) to retrieve waveform data from

REDPy's output .h5 file and produce an interactive plot for picking P-wave arrivals using Seis\_Pick (Verdon, 2012) was adapted to work with our dataset and to allow first motions to be assigned to each P-wave arrival time.

To ensure higher quality analysis, we collected additional station data. We used IRISFetch, a function for MATLAB that gathers data from EarthScope's SAGE database, to obtain waveform data from 11 additional stations within an 8 km radius of the Kīlauea Caldera (Fig. 3) In order to simplify this process, waveform data was obtained for the core event of each cluster of interest instead of producing a new phase-weighted stack of waveforms for all events in a cluster. The core event is the event in each cluster that most closely correlates to each additional event, making it the best depiction of the source and the overall qualities of the cluster. These characteristics associated with the core event allowed us to determine that utilizing additional data for only this event would not heavily reduce the quality of our dataset. P-wave arrivals and first motions were picked once more, this time for up to 18 stations. New arrival time data for the 7 stations that had been previously picked was compared to the original data to ensure correct event timing and determine possible pick uncertainties. A total of 8316 dilatational and 3815 compressional first motions were found.

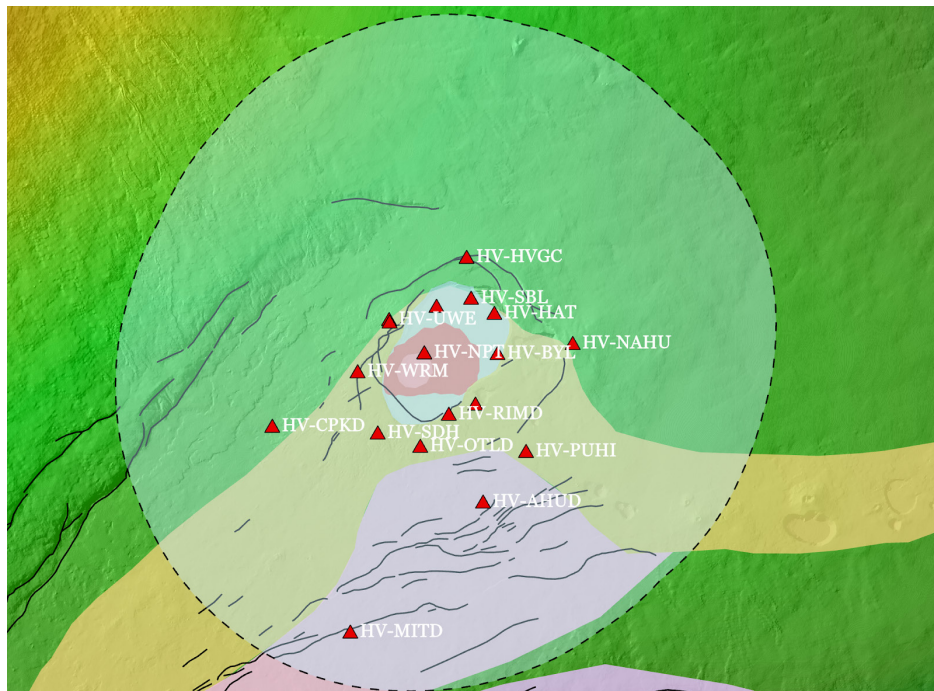


**Figure 3.** A map of HVO stations surrounding the Kīlauea caldera used for this study. The shaded area bounded by dashes represents an 8 km buffer around the caldera, which we deemed the furthest distance acceptable for representative station data.

### 3.3 Earthquake Location

Hypoinverse is an earthquake location program used to locate seismic events. It uses P-wave and S-wave arrival times in conjunction with local crustal models and

station delay files to solve for earthquake hypocenter and origin times. This is a standard approach to earthquake location and is used at HVO for routine processing.

In order to feed the P-wave arrival data associated with first-motion picks for each cluster into Hypoinverse, our data needed to be organized into Hypoinverse archive format (Klein, 2002). Hypoinverse archive format requires cluster event timing, first-motion data, and station data to be organized using specific columns, character lengths, and spacing so that the program can correctly read the values for each attribute (Fig. 4). We created archive files for each cluster, then concatenated them into one phase file to send through the program.

```
201806010401135919 2300155 1600
AHUD HV EHZ PU020180601040114.79
BYL HV HHZ PU020180601040114.09
CPKD HV EHZ PD020180601040115.18
DEVL HV HHZ PD020180601040114.81
HAT HV HHZ PD020180601040114.41
KKO HV HHZ PU020180601040114.13
MITD HV EHZ PU020180601040115.63
OBL HV HHZ PD020180601040114.38
OTLD HV EHZ PD020180601040114.40
PAUD HV HHZ PD120180601040115.09
PUHI HV HHZ PD020180601040114.52
RIMD HV HHZ PD020180601040114.19
RSDD HV EHZ PD020180601040115.27
SBL HV HHZ PD120180601040114.27
SDH HV HHZ PD020180601040114.56
UWB HV HHZ PD020180601040114.38
UWE HV HHZ PD120180601040114.57
WRM HV HHZ PD020180601040114.67
```

**Figure 4.** An example archive file for cluster of interest 343. The first line of the file includes the year, month, day, origin time of the event, latitude, and longitude (both recorded in degrees followed by minutes). Each additional line contains data for a single station including station name, network, channel, P-wave first-motion polarity, and P-wave arrival time.

Jefferson Chang, geophysicist at the Hawaiian Volcano Observatory (HVO), provided the necessary station files, velocity models, and crustal models for running Hypoinverse to locate the earthquakes we identified. Using our phase file along with HVO's data allowed us to produce a summary file, print file, and updated archive file containing the calculated location information for each cluster of interest.

The summary files contained one line for each event processed depicting the date, time, latitude, longitude, depth, RMS, and a grade for the location quality. These summary files were used to map epicenter locations for each cluster of interest using ArcGIS (Fig. 5). The print file lists the parameters used to run the program in addition to printing earthquake data for each cluster. The print files produced were not used for

additional processing and instead acted as storage for parameter documentation. The updated archive files are the exact layout of the original archive files, but the space left for location data has been filled. These new archive files were sent through a focal mechanism software to model possible planes of deformation.

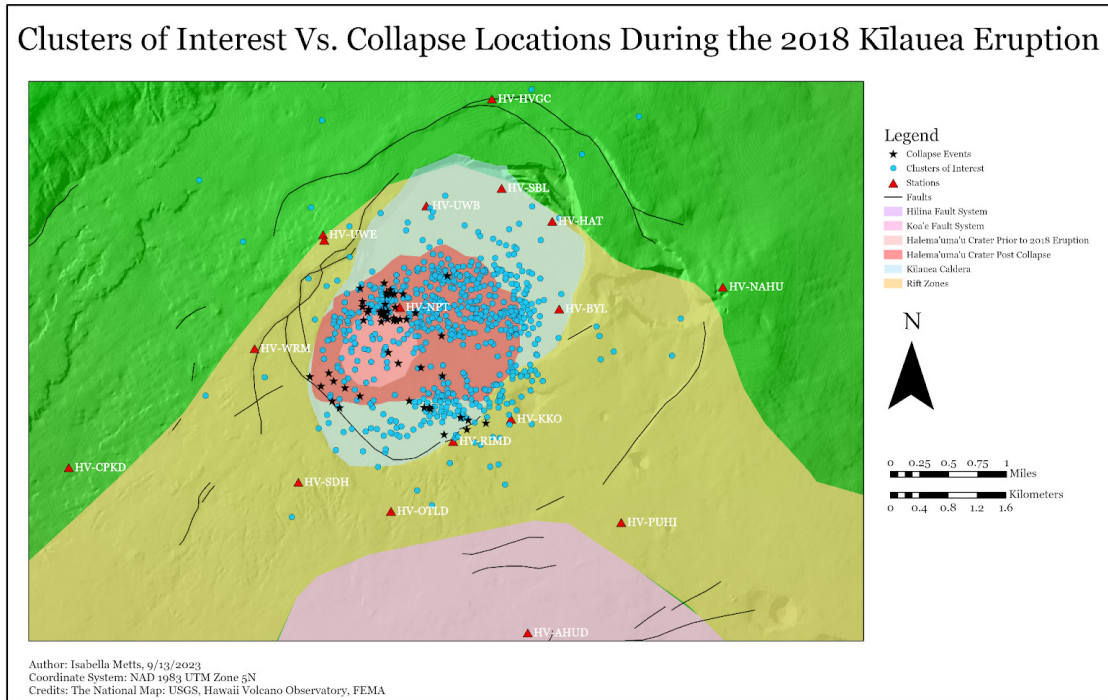


**Figure 5.** A map comparing our cluster of interest locations to the locations of the >M5 earthquakes associated with each collapse event.

### 3.4 Focal Mechanisms

Focal mechanisms are spherical models that depict the orientation and direction of slip along a fault. These simplified models can illustrate double-couple sources where shear failure is represented by the coupling of two forces, a force along a fault plane and an auxiliary plane, to depict a source mechanism. Focal mechanisms can also be used to model non-double-couple events with complex sources involving more than a two-dimensional stress field. The lower half of this spherical model, centered at the hypocenter of an event, is projected onto a 2D stereonet. The stereonets show two possible fault plane orientations, opposite of one another, with identical dipping angles and are shaded by areas of compression and dilatation depending on the direction of slip.

#### 3.4.1 HASH

HASH is a focal mechanism modeling software created by Jeanne Hardebeck and Peter Shearer to produce multiple mechanism solutions for double-couple earthquakes using P-wave first-motion polarities and a grid search method (2002). Of the solutions proposed, grades are given to determine which solution most likely fits the data.

To generate first-motion polarity focal mechanisms HASH requires the first-motion data, location, as well as the takeoff angle for an event. Uncertainties for each of these attributes are also required. The number of acceptable misfit polarities for a solution must be input by the user in addition to sets of acceptable values for the azimuth and takeoff angle. The acceptable range of uncertainties is used to grade the mechanism solutions.

The HASH driver written to accept archive formatted files requires a station polarity reversal file, the input archive file, the output file for focal mechanisms, the output file for acceptable planes, the minimum number of polarities, the maximum azimuthal gap, the maximum takeoff angle, the grid angle for the focal mechanism search, the number of trials, the fraction of picks presumed to be poor, the allowed source-station distance, the angle for computing mechanism probability, and the probability threshold for multiples.

The station polarity reversal file was empty, as no relevant stations were found to be reversed during this eruption sequence. Station reversal was determined by analyzing teleseisms occurring during the eruption sequence and ensuring that the first-motion polarities on all relevant stations were the same. Using large (>5M), deep teleseisms allows for a stronger signal to be recorded and analyzed on stations with a significant distance from the epicenter. For the HVO stations a teleseism occurring in each month of Kīlauea's eruption sequence was analyzed. The 5.3M, 216.6 km Iwanai, Japan earthquake on April 12th, the 5.9M, 585 km Levuka, Fiji earthquake on May 1st, the 5.3M, 113.1km, Kimbe, Papua New Guinea earthquake on June 12th, and the 5.6M, 579 km Suncho Corral, Argentina earthquake on July 20th each produced identical first motions on all HVO stations. The presence of identical first-motion polarities on each station indicates that no stations were reversed during the Kīlauea eruption sequence and that station reversals are not a concern with our dataset.

The input file for HASH was the output archive file from Hypoinverse. The minimum number of polarities was set to 14 out of 18 possible stations while all other inputs were unchanged from the recommended values. The maximum azimuthal gap was left as 90 degrees, the maximum takeoff angle as 60 degrees, the grid angle as 5 degrees, the fraction of presumed poor picks as 10%, the maximum source-station distance as 120km, the angle for computing mechanism probability as 45 degrees, and the probability threshold for multiples as 0.1. Though the fraction of presumed poor picks was left unchanged, the value of 10% matched the pick uncertainty found when adding additional stations to the dataset, re-picking first motions, and assessing any polarity discrepancies between the first and second picks.

The files output from HASH indicated that the focal mechanism quality was very low, with grades ranging from B-Z. The focal planes produced by HASH were modeled using a Matlab script written by Cristhian Salas Pazmiño (2021). The resulting focal mechanism models presented a large percentage of mismatching stations (Fig. 6), indicating that none of the events were true double couple events (Appendix A.2) and that focal mechanism modeling through HASH would not, alone, be valuable towards understanding the eruption sequence. Future work could aim to create moment tensors for these families to understand more about their non-double couple sources.

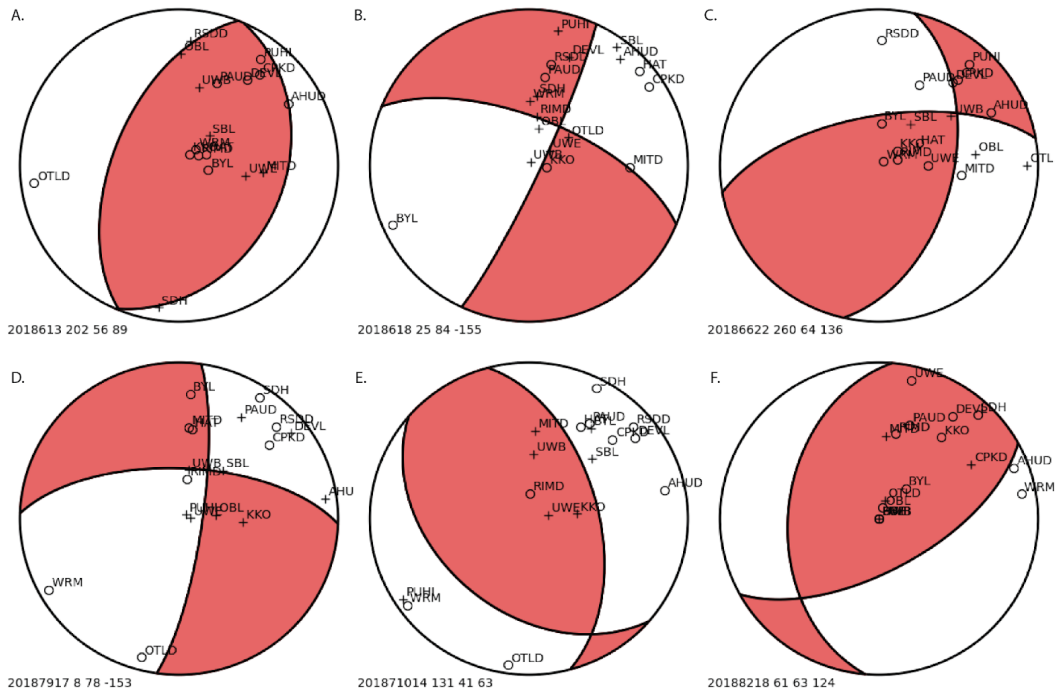


**Figure 6.** Focal mechanism planes produced by HASH and modeled using a Matlab script written by Cristhian Salas Pazmiño (2021). These models depict mismatched station polarities, where station polarity does not match the region of compression or dilatation that the station is plotted within. In this example, open circles and white regions represent dilatation while crosses and red regions represent compression. Where open circles are plotted in red regions and crosses are plotted in white regions, the stations are considered “mismatched”.



## 4 Data

### 4.1 Repeating Events

Over 167,000 seismic events between April 29th and August 2nd, 2018 were cataloged and organized into nearly 6,000 families using REDPy. A dramatic change in waveform characteristics of collapse events and an increase in higher frequency seismic energy occurred on May 29th, co-occurring with the introduction of almost daily collapse events. The inter-collapse microseismicity also changed on this day: all active families ceased and 50 new families began (Fig. 7). With the onset of these new families, a pattern emerges showing a steady increase in the number of repeating events per hour prior to a summit collapse and a seismic reset with the onset of collapse. After a collapse event occurs the number of repeating earthquakes per hour drops and then begins to rise again as the cyclic collapses continue (Fig. 8). This pattern indicates that the rise in repeating earthquakes per hour may contribute to the collapse event or even act as a warning with repeating seismic events being triggered by the same sources as the collapse itself.

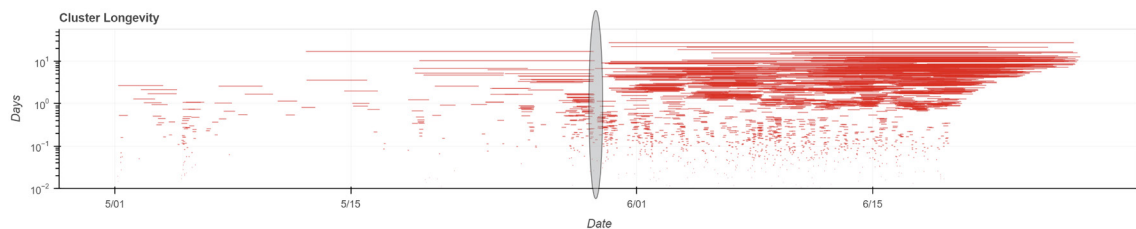


**Figure 7.** Cluster longevity plot for repeating events in catalog C1 highlighting the termination of all active families on May 29<sup>th</sup> in gray.

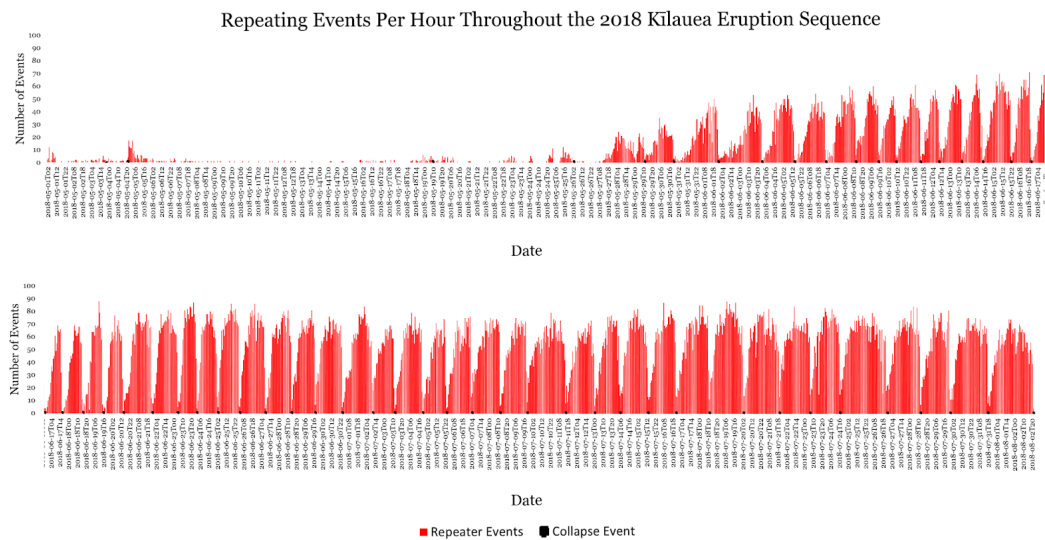


**Figure 8.** Timeline depicting repeating events per hour for the duration of caldera collapse events throughout the 2018 eruption sequence. Collapse events occurred from the beginning of May through August 2<sup>nd</sup> and are depicted as black points on the timeline. A distinct pattern of repeating events per hour increasing prior to collapse emerges with the onset of near-daily collapse events.

Of the new families to emerge on May 29th after all original families ceased, the majority recorded their final event within 48 hours. Despite cyclically occurring explosive collapses, some families persist for multiple days. Families that persist through collapse events suggest a source independent of summit deformation, but one that may still impact collapse mechanics. Families that are continuously triggered indicate dominant sources during the eruption sequence that may be key to understanding seismic cycles. For this reason, family longevity and event quantity are the chosen parameters for our clusters of interest. As the eruption sequence continued 21 families were found that contained more than 100 events, 552 families were found to persist 7 days or more, and 103 families were found to share both qualities. We manually picked P-wave arrival times and first-motion polarities for the 676 qualifying clusters of interest. Each cluster included waveform data from 18 stations, though not all stations for all clusters were deemed pickable. Out of a possible 12168 P-wave arrivals, we picked 12131. Of these 12131, 8316 (69%) were dilatational and 3815 (31%) were compressional. Shelly and Thelen (2019) found that dilatational first motions also dominated the HVO earthquake catalog used for their study with 67% of first motions being dilatational and 33% compressional. Stations recording dilatational first motions depict areas of pressure towards the hypocenter, while stations recording compressional first motions depict areas of extension away from the hypocenter. Dilatational dominance is indicative of a negative volumetric change source component, such as the closure of cracks (Shelly & Thelen, 2019). Clusters with >80% dilatational first motions (Appendix A.3) were labeled as “crack-closing” events through analysis of source type models (Fig. 9) and their placement of purely dilatational and purely compressional events in regions of crack-closing and crack-opening sources, respectively. The Fundamental lobe is split into two hemispheres, the upper hemisphere representing a positive volume change and the lower hemisphere representing a negative volume change (Lanza & Waite, 2018). Isotropic (ISO) source end-members, representing explosive and implosive sources that consist purely of volumetric change and produce homogeneous P-wave polarities, exist at each upper and lower margin of the lobe. Compensated linear vector dipole (CLVD) and double-couple (DC) sources do not have a component of net volumetric change, separating them from ISO sources and placing them in the center of the lobe. DC sources tend to have a mix of P-wave polarities due to the two contradicting forces driving source mechanisms. In a perfect DC mechanism, 50% of first-motion polarities would be dilatational and 50% compressional. The range from a 50% split between first-motion polarities in the center of the lobe and the purely dilatational or compressional polarities associated with each ISO endmember has allowed us to estimate that clusters with >80% dilatational first motions fall into the region associated with crack-closing sources. If these events do represent crack-closing sources, they would be placed in the southern hemisphere of the lobe along the crack source arc (Fig. 9).

Of the 676 clusters of interest, 181 (27%) were deemed to be “crack-closing” (Fig. 10), though additional events with less than 80% dilatational first motions may still fall along the crack source arc if locations along the lobe were calculated. These “crack-closing” events could represent conduit collapse following magma drainage or the closing of fractures resulting from slip along a concave surface.

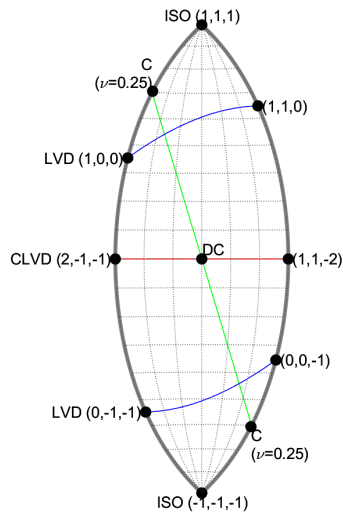


**Figure 9.** Fundamental Lune model depicting source types and the moment tensor eigenvalues that correspond with them (adapted from Tape & Tape, 2012). Isotropic (ISO), crack (C), linear vector dipole (LVD), compensated linear vector dipole (CLVD), and double-couple (DC) components are plotted on the lune. Blue lines represent the boundary where all focal spheres above the positive hemisphere arc are completely compressional (all red) and all below the negative hemisphere arc are completely dilatational (all white). The red line indicates the lunes deviatoric arc, and the green line is the arc for crack sources with double couple components (Tape & Tape, 2012).

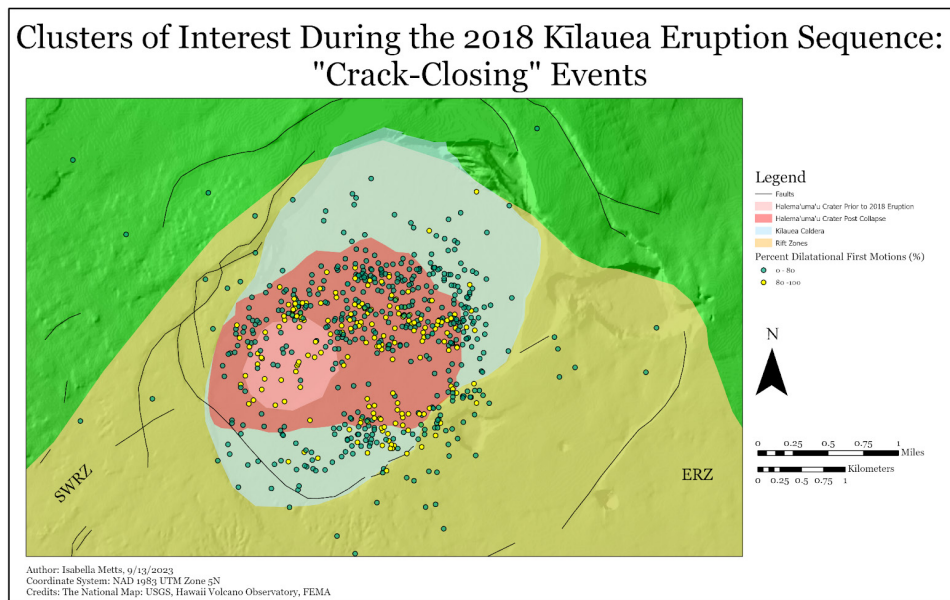


**Figure 10.** A map of our clusters of interest color coded by the percentage of first-motion polarities that are dilatational. Events plotted in yellow represent “crack-closing” events.

## 4.2 Mean Frequency Index

In addition to longevity and event quantity, mean frequency data was retrieved from individual cluster pagers produced by REDPy. The frequency index for a seismic event is calculated by finding the logarithm of the ratio between the mean of spectral amplitudes across a high ( $A_{up}$ ) and low ( $A_{low}$ ) frequency band. The resulting value is beneficial in categorizing clusters using frequency-based classifications such as LP, hybrid, and VT.

$$FI = \log_{10} \frac{\text{mean}(A_{up})}{\text{mean}(A_{low})}$$

For the entire catalog, 6153 families of repeating events, mean frequency index values range from -0.94 to 0.49, with a mean of -0.05, a median of -0.01, and a mode of 0.13. Considering only our clusters of interest, mean frequency index values range from -0.8 to 0.37, with a mean of -0.04, a median of 0.01, and a mode of 0.01 (Fig. 11).

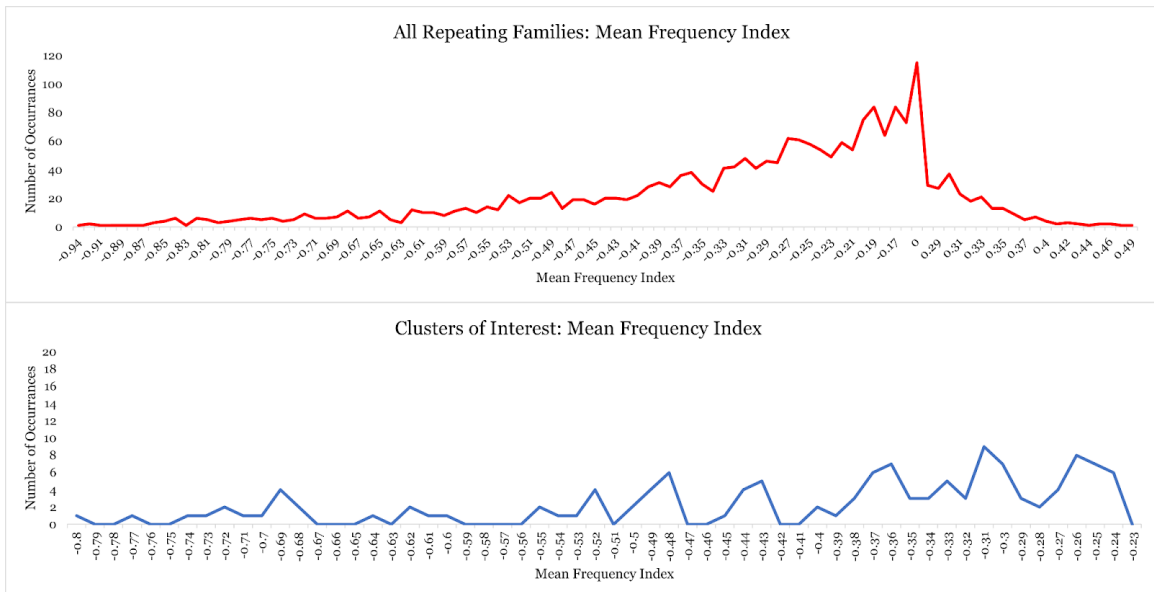


**Figure 11.** Number of occurrences of mean frequency index values within the entire catalog (red) and within only our clusters of interest (blue).

The correlation between frequency index values and frequency-based classifications varies based on the frequency bands used for calculation. REDPy documentation states that, when using the default values for low and high frequency bands, frequency index values above 0 tend to represent tectonic events while those below 0 more closely resemble long period events. The default values used for frequency index windows were a low frequency range,  $A_{low}$ , of 1 - 2.5 Hz and a high frequency range,  $A_{up}$ , of 5-10 Hz. To ensure that 0 was a reasonable boundary between LP and VT events, spectral plots of clusters with frequency index values less than 0, equal to 0, and more than 0 were analyzed (Fig. 12).

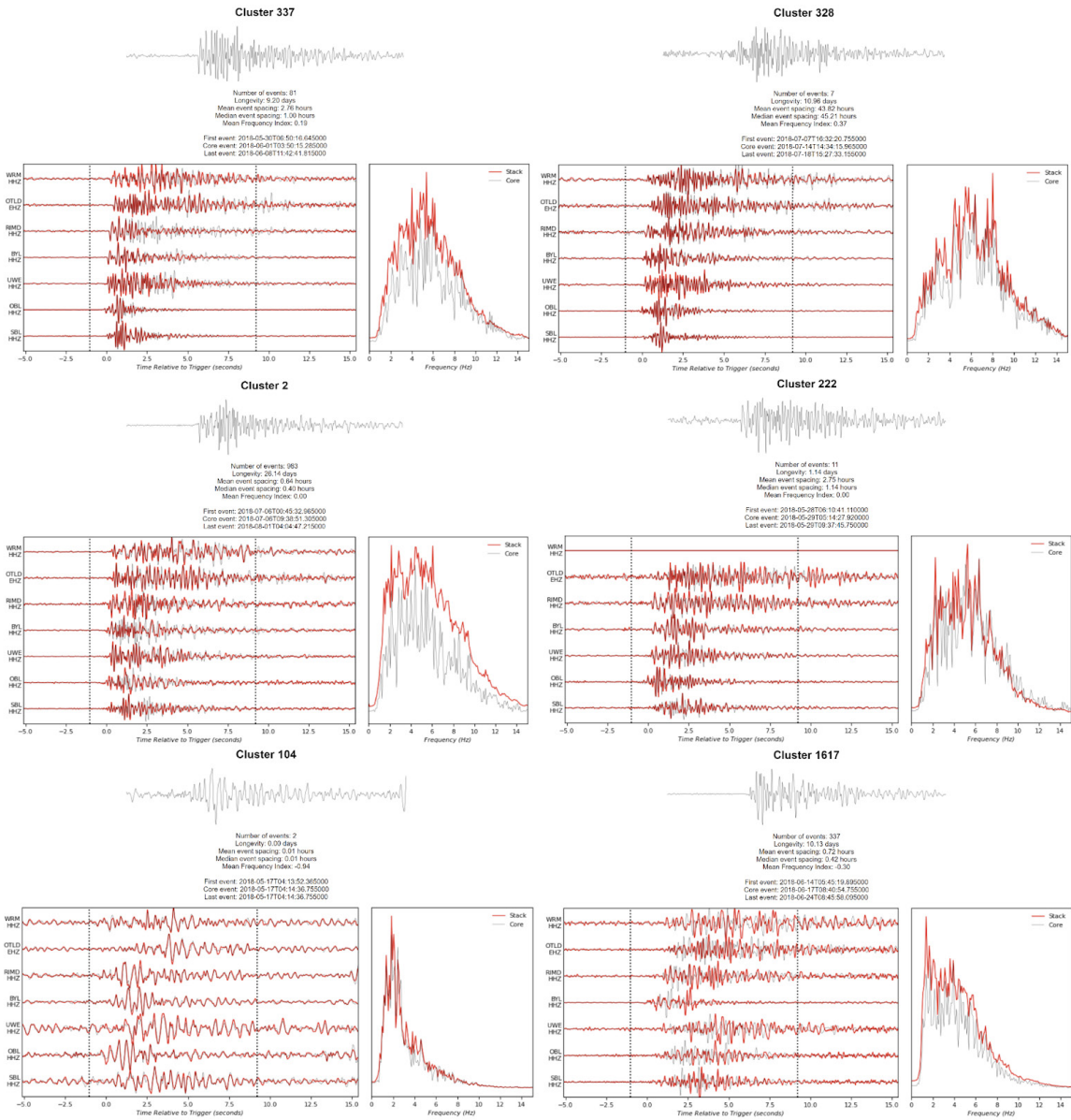


**Figure 12.** REDPy produced spectral plots of clusters with mean frequency index (FI) values  $>0$  (clusters 337 & 328), clusters with mean FI values equal to 0 (clusters 2 & 222), and clusters with mean FI values  $<0$  (clusters 104 & 1617). These plots are accompanied by waveform data for each station to the left of the spectral plot and a representative core waveform beneath each cluster title.

Spectral plots for events with frequency index values greater than 0 show an increase in amplitudes at higher frequencies when compared to events with frequency index values less than 0. These spectral plots align with the expected frequency distributions for VT, Hybrid, and LP classifications. Higher spectral amplitudes in VT signals typically range from 5-10 Hz and waveforms often present impulsive first motions, both of which are similar to what the spectral plots for clusters with frequency index values greater than 0. Higher spectral amplitudes in LP signals typically range from

0.5-5 Hz and waveforms often present acoustic resonance following the onset of an event, both of which are attributes of the spectral plots for clusters with frequency index values less than 0. The spectral plots associated with frequency index values of 0 have a wider range of frequencies where high amplitudes are recorded and the associated waveforms show resonance as well as possible tectonic onsets, indicating that clusters with these frequency index values are likely hybrid events.

Grouping hybrid events with LP events, as hybrid waveforms are more closely related to the shear onset and resonance seen in LP's than the impulsive events in VT's, leaves us with two categories for analyzing our clusters of interest. Clusters with frequency index values less than or equal to 0 are compared to clusters of interest with frequency index values greater than 0. Those with frequency index values greater than 0 are considered to have some form of brittle failure associated with the event source, while those with frequency index values less than or equal to zero are more likely to have sources associated with fluid transportation and the opening and closing of fluid filled cracks.

Clusters with frequency index values less than or equal to 0 are dispersed across the Kīlauea caldera region, where clusters with frequency index values greater than zero are more congested to the area north-east of the Halema'uma'u crater. Congestion of these brittle failure, VT, events follows the direction of crater expansion over the course of the eruption sequence (Fig 13). Throughout the 2018 eruption sequence these higher frequency events were mostly absent from the original Halema'uma'u Crater as well as a small gap towards the east (Fig. 14). Lower frequency events were more common in and around the Halema'uma'u crater, likely due to the magmatic activity centered in this region.

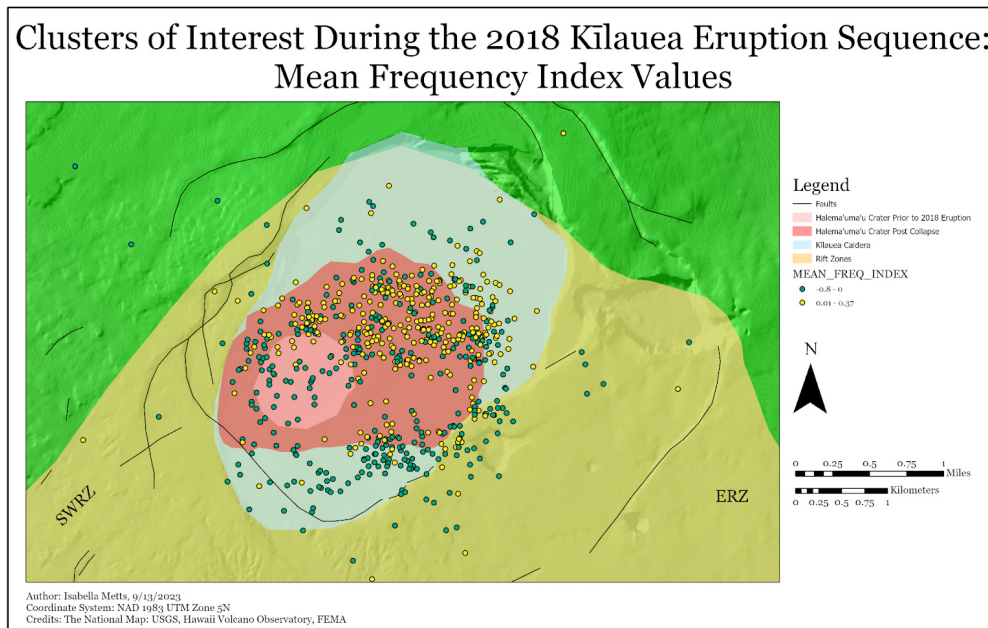


**Figure 13.** A map of our clusters of interest color coded by their mean frequency index (FI) values. Events plotted in yellow have FI values greater than 0, while events plotted in green have FI values less than or equal to 0.

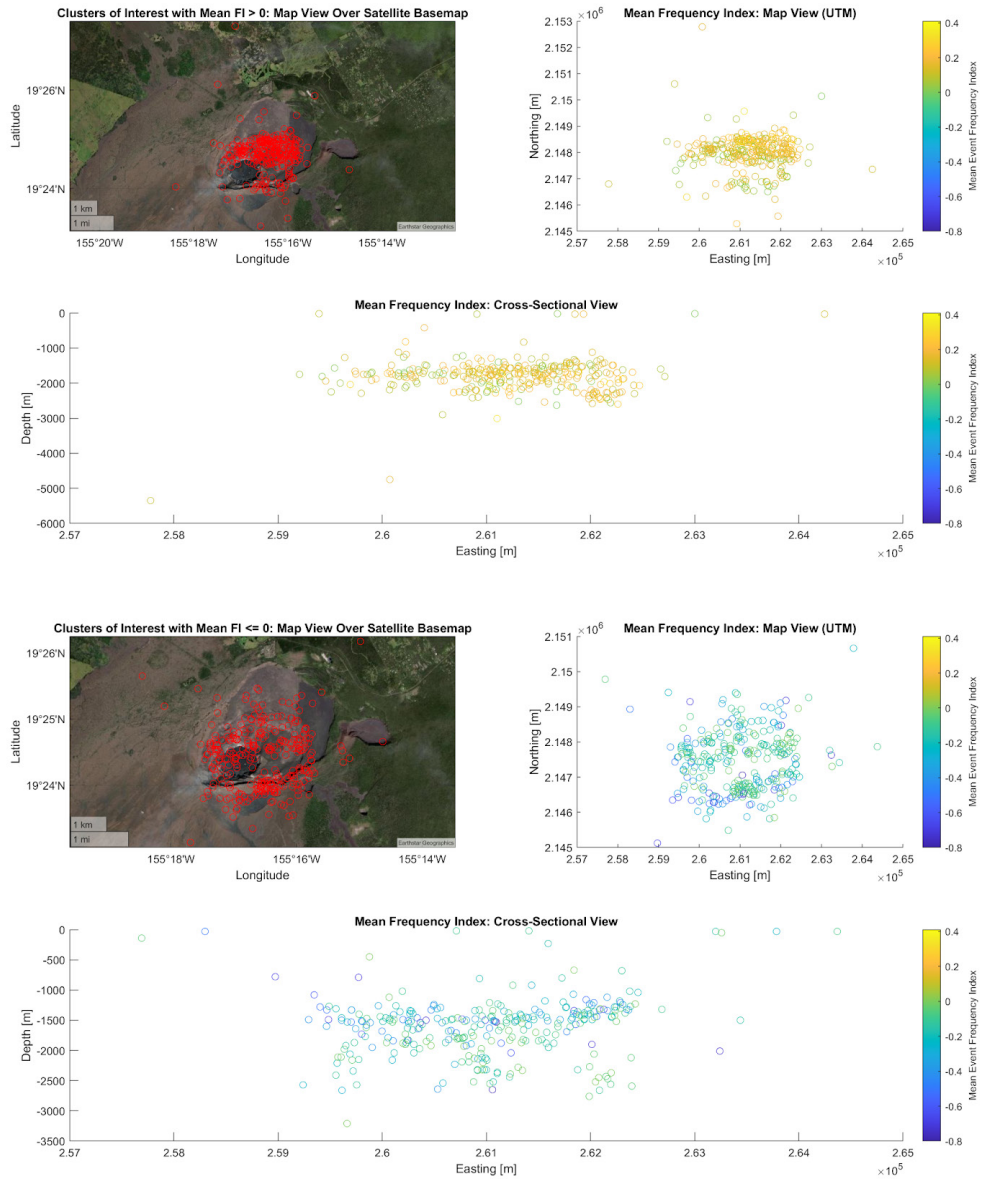


**Figure 14.** Map view and cross-section of our clusters of interest, again color coded by FI value. Events with FI values greater than 0 have been separated from those with FI values less than or equal to 0 for ease of comparison.

Separating clusters of interest by their qualifying attributes leaves three categories: longevity clusters, event quantity clusters, and clusters with both attributes. Of these categories, 52% of clusters chosen for their longevity, 19% of clusters chosen for their event quantity, and 46% of clusters with both qualities had mean frequency index values greater than 0. Clusters that continue to repeat over a long period of time likely represent repeated slip on a fault, where clusters with more than 100 events in a shorter period of time may be indicative of continual fluid movement through a network of conduits.

The post-collapse Halema'uma'u crater is bounded by a ring fault system, most of which is hypothesized to have developed during the 2018 eruption sequence (Wang et al., 2023). Volcano tectonic event locations, cataloged by Wang et al., align with the eastern expansion of the ring fault system (2023). Catalogs produced by Wang et al. use a much higher correlation coefficient than our catalog, producing fewer repeating clusters and centralizing these clusters along the ring fault boundary (2023). The large number of brittle failure source clusters in our catalog spanning across the new crater, especially those chosen for their longevity attributes, may be indicative of crater expansion as well as growth and creep along this ring fault system.

### 4.3 Focal Mechanisms

The models we produced provide valuable insight despite the focal mechanisms from HASH containing high numbers of mismatched stations. Mismatched station first motions indicate that our events do not fit the double-couple model that HASH produces and are instead non-double-couple events. Non-double-couple events are rare globally; fewer than 10% of the earthquakes cataloged by the International Seismological Centre contain enough mismatched stations to bar source determination using double-couple mechanisms (Lentas et al., 2019).

Though the first-motion polarities are not consistent with double-couple events, they depict a consistent pattern with dilation everywhere except for a circular compressional zone in the northeast (Fig. 15). One interpretation of this is reverse slip on a curved fault, such as a portion of a ring fault. This mechanism is nearly opposite from the normal motion associated with the caldera collapse events.

Moment tensors produced by the USGS for the >M5 earthquake events associated with each collapse also suggest slip on a curved fault (Fig. 16). The USGS models show a dilatational zone surrounded by a zone of compression, indicating normal ring faulting. Comparing our mechanisms to those produced by the USGS suggests that fault motion is reversed between collapses. The mechanisms for the microseismicity suggest shortening to account for large volumes of material being forced into regions of less volume during a collapse (Fig. 17). Reverse faulting along outward-dipping ring fault boundaries has been reproduced in experimental models of incremental caldera collapse (Ruch et al., 2012) and is predicted by numerical models (Segall et al., 2019).



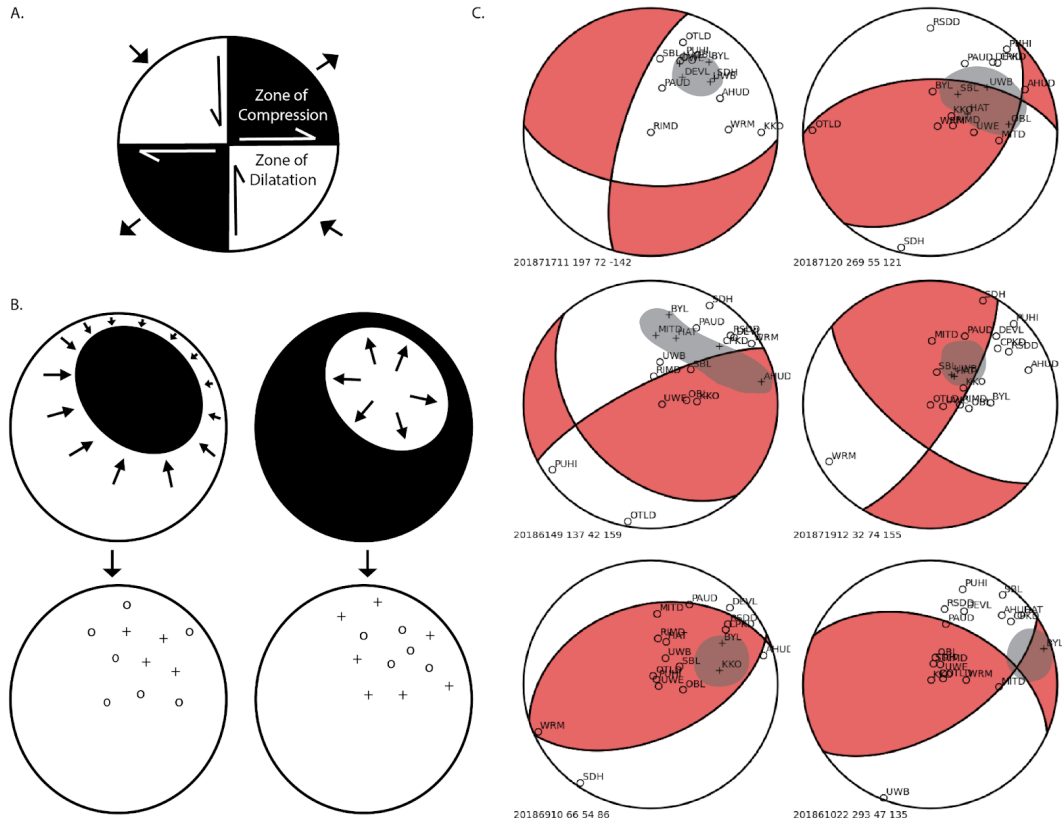


**Figure 15.** (a) An example of a double couple focal mechanism depicting a left lateral strike-slip fault and the accompanying zones of compression and dilatation. (b) A focal mechanism depicting a ring fault structure, the accompanying zones of dilatation and compression, and an example of this structure using open circles and crosses instead of color-coded zones (adapted from Shuler, 2013). The left mechanism represents a reverse ring fault, while the mechanism on the right represents a normal ring fault. (c) Six examples of our mismatched, non-double-couple, focal mechanisms that present this ring fault structure (highlighted in gray) when inaccurate color-coded regions are ignored and only the location of open circles and crosses are taken into consideration.

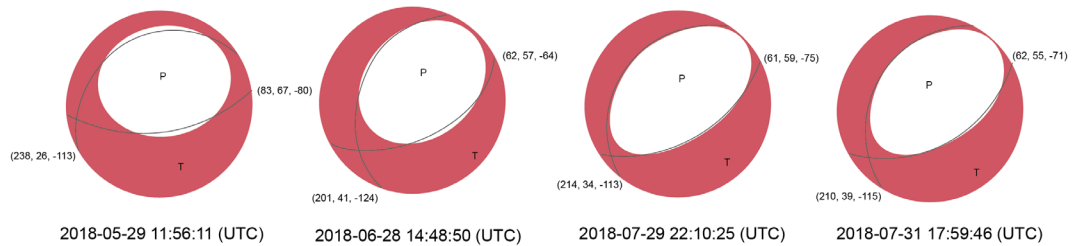


**Figure 16.** Moment tensors for four  $>M5$  earthquakes associated with caldera collapse events modeled by the USGS depicting normal ring faulting (adapted from Earthquake Hazards Program – USGS, 2018).

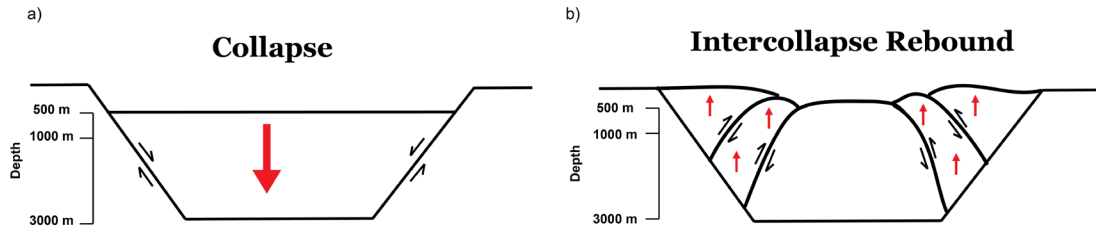


**Figure 17.** Proposed ring fault motion throughout the collapse sequence. (a) The figure on the left depicts normal ring faulting during collapse. Hypocenters associated with the collapse events were calculated by the USGS to be around 200 m depth, while total subsidence reached 500 m depth. (b) The figure on the right depicts reverse ring faulting to accommodate the reduced caldera diameter with depth. Material propagates upward as a response to large volumes of material collapsing into a smaller volume area. Hypocenters associated with our clusters of interest were calculated to occur most often between depths 1000 m and 3000 m.

## 5 Conclusions

The significant amount of data available for Kīlauea’s 2018 eruption and subsequent comprehensive caldera collapse has made Kīlauea a notable study region for caldera seismology. We produced an event catalog, including previously overlooked microseismicity, of more than 167,000 recognized events and assembled almost 6,000 families of repeating earthquakes to study repetitive sources and their relationship to caldera collapse mechanics. Of the 6,000 families found, 676 were deemed “clusters of interest” based on cluster longevity and event quantity. P-wave arrivals and first-motion polarities were manually picked on stacked traces for each cluster of interest on up to 18 stations within an 8 km radius of the Kīlauea caldera. First-motion polarities were used to locate event hypocenters and assess possible source mechanisms. HASH, a double-couple focal mechanism modeling software, was used to produce focal mechanisms for the clusters of interest resulting in proof that these events are not actually results of double-couple sources and increasing the importance of our source estimates based on first-motion polarity and waveform analysis.

The dominance of dilatational first motions noted in previous studies as indicative of crack-closing sources with a negative volumetric change component (Shelly & Thelen, 2019), can alternatively be interpreted as slip on dipping curved faults. The location of clusters with more than 80% dilatational first motions across the region of the Halema‘uma‘u crater’s eastern expansion indicates that these events may be the result of the slight subsidence occurring as magma moves out of the northeastern conduits and the crater expands.

Frequency index values for our clusters of interest indicate that volcano tectonic events occur outside of the original Halema‘uma‘u crater and across the region of eastern expansion towards the new crater boundary. These VT events likely represent repetitive slip along a growing ring fault structure as cyclical collapse continues and forms a new crater and fault structure. LP events are more spread out within the caldera, likely representing fluid movement through magmatic networks and the hydrothermal system northeast of the original Halema‘uma‘u crater.

The focal mechanisms we produced, despite displaying mismatched station polarities that did not fit our double-couple model, provided a model depicting the ring fault structure that the localized VT seismicity stems from. Slip along a growing curved ring fault accounts for events not fitting a double-couple model, repetitive trigger of the same source over time, and crack closing signals. As this ring fault structure evolved during the expansion of the Halema‘uma‘u crater, which it bounds, microseismicity and repetitive events followed. During inter-collapse periods reverse ring faulting dominated source mechanics with material propagating upwards as a way to accommodate the reduced caldera diameter at depth.

Future work should aim to calculate moment tensors for this catalog to further analyze the forces involved behind event source mechanisms. Focal mechanisms modeled for non-double-couple events should be able to tell us more about the ring fault structure and its evolution throughout the eruption sequence. Understanding the relationship between inter-collapse seismicity and slip along this ring fault structure can provide insight on the connection between ring fault growth, collapse events, and rebound mechanics. Using moment tensor eigenvalues to properly plot sources on the

fundamental lune will enhance our understanding of more complicated sources that could not be inferred by first-motion polarities and waveform analysis, specifically the less studied LP events.

## 6 Reference List

- Acocella, V. (2007). Understanding caldera structure and development: An overview of analogue models compared to natural calderas. *Earth-Science Reviews*, 85(3–4), 125–160. <https://doi.org/10.1016/j.earscirev.2007.08.004>
- Almendros, J., Chouet, B., & Dawson, P. (2001). Spatial extent of a hydrothermal system at Kīlauea Volcano, Hawaii, determined from array analyses of shallow long-period seismicity: 2. results. *Journal of Geophysical Research: Solid Earth*, 106(B7), 13581–13597. <https://doi.org/10.1029/2001jb000309>
- Brill, Kyle, 2019, "Seismic Signals and Sources at Fuego Volcano, Guatemala During January 2012", Open Access Dissertation, Michigan Technological University. <https://doi.org/10.37099/mtu.dc.etr/784>
- Calvert, A. T., & Lanphere, M. A. (2006). Argon geochronology of Kīlauea's early submarine history. *Journal of Volcanology and Geothermal Research*, 151(1–3), 1–18. <https://doi.org/10.1016/j.jvolgeores.2005.07.023>
- Chouet, B. A., & Matoza, R. S. (2013). A multi-decadal view of seismic methods for detecting precursors of magma movement and eruption. *Journal of Volcanology and Geothermal Research*, 252, 108–175. <https://doi.org/10.1016/j.jvolgeores.2012.11.013>
- Duffield, W. A. (1975). Structure and origin of the Koa'e Fault System, Kīlauea Volcano, Hawaii. *U. S. Geological Survey Professional Paper*, 856. <https://doi.org/10.3133/pp856>
- Earthquake Hazards Program (2018). U.S. Geological Survey (USGS). U.S. Department of the Interior, United States.
- Ge, S., Lin, G., Amelung, F., Okubo, P. G., Swanson, D. A., & Yunjun, Z. (2019). The accommodation of the South Flank's motion by the Koa'e Fault System, Kīlauea, hawai'i: Insights from the June 2012 earthquake sequence. *Journal of Geophysical Research: Solid Earth*, 124(11), 11116–11129. <https://doi.org/10.1029/2018jb016961>
- Gudmundsson, Magnús T., et al. "Gradual caldera collapse at Bárðarbunga volcano, Iceland, regulated by lateral magma outflow." *Science*, vol. 353, no. 6296, 2016, <https://doi.org/10.1126/science.aaf8988>
- Hardebeck, J. L., & Shearer, P. M. (2002). A new method for determining first-motion focal mechanisms. *Bulletin of the Seismological Society of America*, 92(6), 2264–2276. <https://doi.org/10.1785/0120010200>

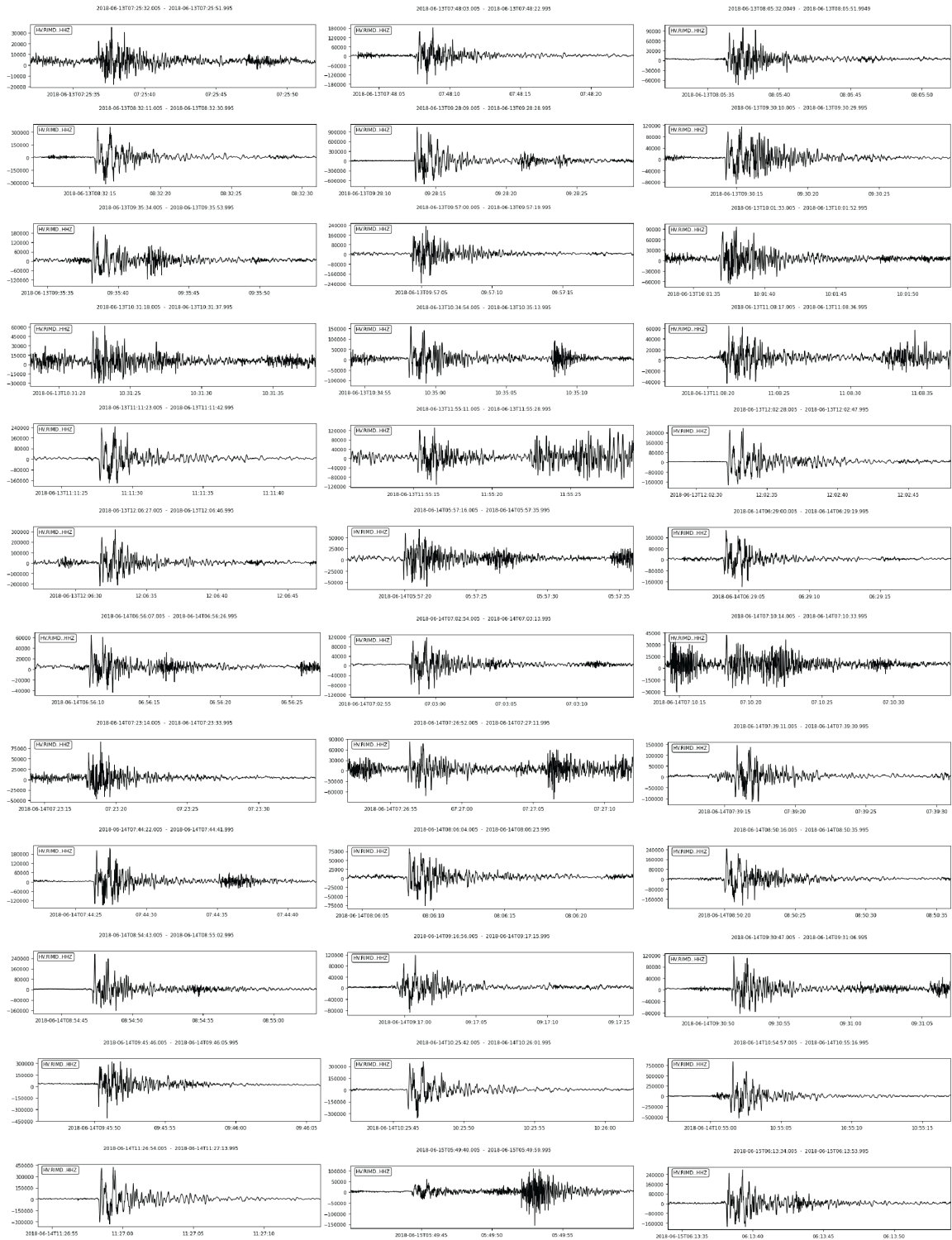
- Holcomb, R. T. (1987). Eruptive History and Long-term Behavior of Kīlauea Volcano (Hawaii). *U.S. Geological Survey Professional Paper*, 1350(1).
- Hotovec-Ellis, A. J., & Jeffries, C. (2016). Near Real-time Detection, Clustering, and Analysis of Repeating Earthquakes: Application to Mount St. Helens and Redoubt Volcanoes – Invited. Paper presented at the Seismological Society of America Annual Meeting, Reno, Nevada. <https://github.com/ahotovec/REDPy>
- Kauahikaua, J. (1993). Geophysical Characteristics of the Hydrothermal System of Kīlauea Volcano, Hawai'i. *Geothermics*, 22(4), 271–299.
- Klein, F. W. (2002). User's Guide to hypoinverse-2000, a FORTRAN program to solve for earthquake locations and magnitudes. *Open-File Report*. <https://doi.org/10.3133/ofr02171>
- Kumagai, H., Chouet, B. A., & Dawson, P. B. (2005). Source process of a long-period event at Kīlauea Volcano, Hawaii. *Geophysical Journal International*, 161(1), 243–254. <https://doi.org/10.1111/j.1365-246x.2005.02502.x>
- Lanza, F., & Waite, G. P. (2018). A nonlinear approach to assess network performance for moment-tensor studies of long-period signals in volcanic settings. *Geophysical Journal International*, 215(2), 1352–1367. <https://doi.org/10.1093/gji/ggy338>
- Lentas, Konstantinos, et al. (2019). “The ISC bulletin as a comprehensive source of earthquake source mechanisms.” *Earth System Science Data*, vol. 11, no. 2, pp. 565–578, <https://doi.org/10.5194/essd-11-565-2019>.
- Lipman, P. W., Lockwood, J. P., Okamura, R. T., Swanson, D. A., & Yamashita, K. M. (1985). Ground Deformation Associated with 1975 Magnitude- 7.2 Earthquake and Resulting Changes in Activity of Kīlauea volcano, Hawaii. *U. S. Geological Survey Professional Paper*, 1276.
- Lipman, P. W., Sisson, T. W., Ui, T., Naka, J., & Smith, J. R. (2002). Ancestral submarine growth of Kīlauea Volcano and instability of its south flank. *Hawaiian Volcanoes: Deep Underwater Perspectives*, 161–191. <https://doi.org/10.1029/gm128p0161>
- MATLAB Release 2022a, The MathWorks, Inc., Natick, Massachusetts, United States.
- Nehlig, P. (1991). Salinity of oceanic hydrothermal fluids: A fluid inclusion study. *Earth and Planetary Science Letters*, 102(3–4), 310–325. [https://doi.org/10.1016/0012-821x\(91\)90026-e](https://doi.org/10.1016/0012-821x(91)90026-e)

- Okubo, P. G., Nakata, J. S., & Koyanagi, R. Y. (2014). The evolution of seismic monitoring systems at the Hawaiian Volcano Observatory. *Professional Paper*, 67–94. <https://doi.org/10.3133/pp18012>
- Parfitt, E. A., & Peacock, D. C. P. (2001). Faulting in the south flank of Kīlauea Volcano, Hawai‘i. *Journal of Volcanology and Geothermal Research*, 106(3–4), 265–284. [https://doi.org/10.1016/s0377-0273\(00\)00247-x](https://doi.org/10.1016/s0377-0273(00)00247-x)
- Podolsky, D. M. W., & Roberts, G. P. (2008). Growth of the volcano-flank Koa‘e Fault System, Hawaii. *Journal of Structural Geology*, 30(10), 1254–1263. <https://doi.org/10.1016/j.jsg.2008.06.006>
- Ruch, J., et al. “Kinematic analysis of vertical collapse on volcanoes using experimental models time series.” *Journal of Geophysical Research: Solid Earth*, vol. 117, no. B7, 2012, <https://doi.org/10.1029/2012jb009229>.
- Salas Pazmiño, Cristhian, 2021, "Seismotectonic Interpretation of an Expansive Set of Earthquake Focal Mechanisms from First Motions and Amplitude Ratios on the Yellowstone Plateau" Open Access Master's Thesis, Michigan Technological University. <https://doi.org/10.37099/mtu.dc.etr/1233>
- Segall, Paul, et al. “Mechanics of inflationary deformation during caldera collapse: Evidence from the 2018 kīlauea eruption.” *Geophysical Research Letters*, vol. 46, no. 21, 2019, pp. 11782–11789, <https://doi.org/10.1029/2019gl084689>.
- Shelly, D. R., & Thelen, W. A. (2019). Anatomy of a caldera collapse: Kīlauea 2018 summit seismicity sequence in high resolution. *Geophysical Research Letters*, 46(24), 14395–14403. <https://doi.org/10.1029/2019gl085636>
- Shuler, A., Ekström, G., & Nettles, M. (2013). Physical mechanisms for vertical-CLVD earthquakes at active volcanoes. *Journal of Geophysical Research: Solid Earth*, 118(4), 1569–1586. <https://doi.org/10.1002/jgrb.50131>
- Swanson, D. A., Rose, T. R., Mucek, A. E., Garcia, M. O., Fiske, R. S., & Mastin, L. G. (2014). Cycles of explosive and effusive eruptions at Kīlauea Volcano, Hawai‘i. *Geology*, 42(7), 631–634. <https://doi.org/10.1130/g35701.1>
- Tape, W., & Tape, C. (2012). A geometric setting for moment tensors. *Geophysical Journal International*, 190(1), 476–498. <https://doi.org/10.1111/j.1365-246x.2012.05491.x>
- Verdon, J. (2012). Seis\_Pick. MATLAB Central File Exchange - <https://www.mathworks.com/matlabcentral/fileexchange/34941-seis-pick>. Retrieved from <https://www.mathworks.com/matlabcentral/fileexchange/34941-seis-pick>

- Wang, K., MacArthur, H. S., Johanson, I., Montgomery-Brown, E. K., Poland, M. P., Cannon, E. C., d'Alessio, M. A., & Bürgmann, R. (2019). Interseismic quiescence and triggered slip of active normal faults of Kīlauea Volcano's south flank during 2001–2018. *Journal of Geophysical Research: Solid Earth*, *124*(9), 9780–9794. <https://doi.org/10.1029/2019jb017419>
- Wang, T. A., Segall, P., Hotovec-Ellis, A. J., Anderson, K. R., & Cervelli, P. F. (2023). Ring fault creep drives volcano-tectonic seismicity during caldera collapse of Kīlauea in 2018. *Earth and Planetary Science Letters*, *618*, 118288. <https://doi.org/10.1016/j.epsl.2023.118288>
- Wilding, J. D., Zhu, W., Ross, Z. E., & Jackson, J. M. (2023). The magmatic web beneath hawai'i. *Science*, *379*(6631), 462–468. <https://doi.org/10.1126/science.ade5755>
- Zurek, J., & Williams-Jones, G. (2013). The shallow structure of Kīlauea caldera from high-resolution Bouguer gravity and total magnetic anomaly mapping: Insights into Progressive Magma Reservoir Growth. *Journal of Geophysical Research: Solid Earth*, *118*(7), 3742–3752. <https://doi.org/10.1002/jgrb.50243>







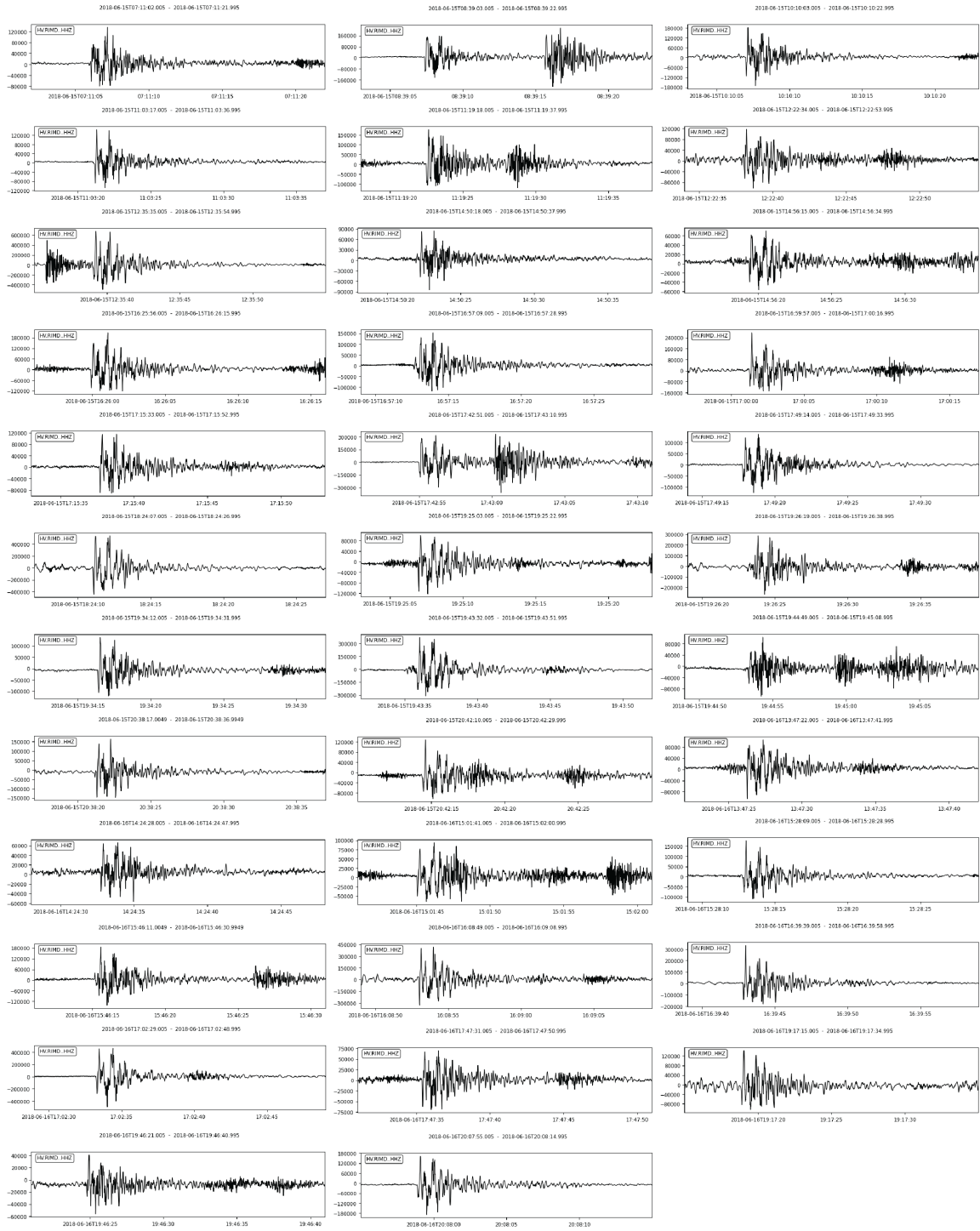
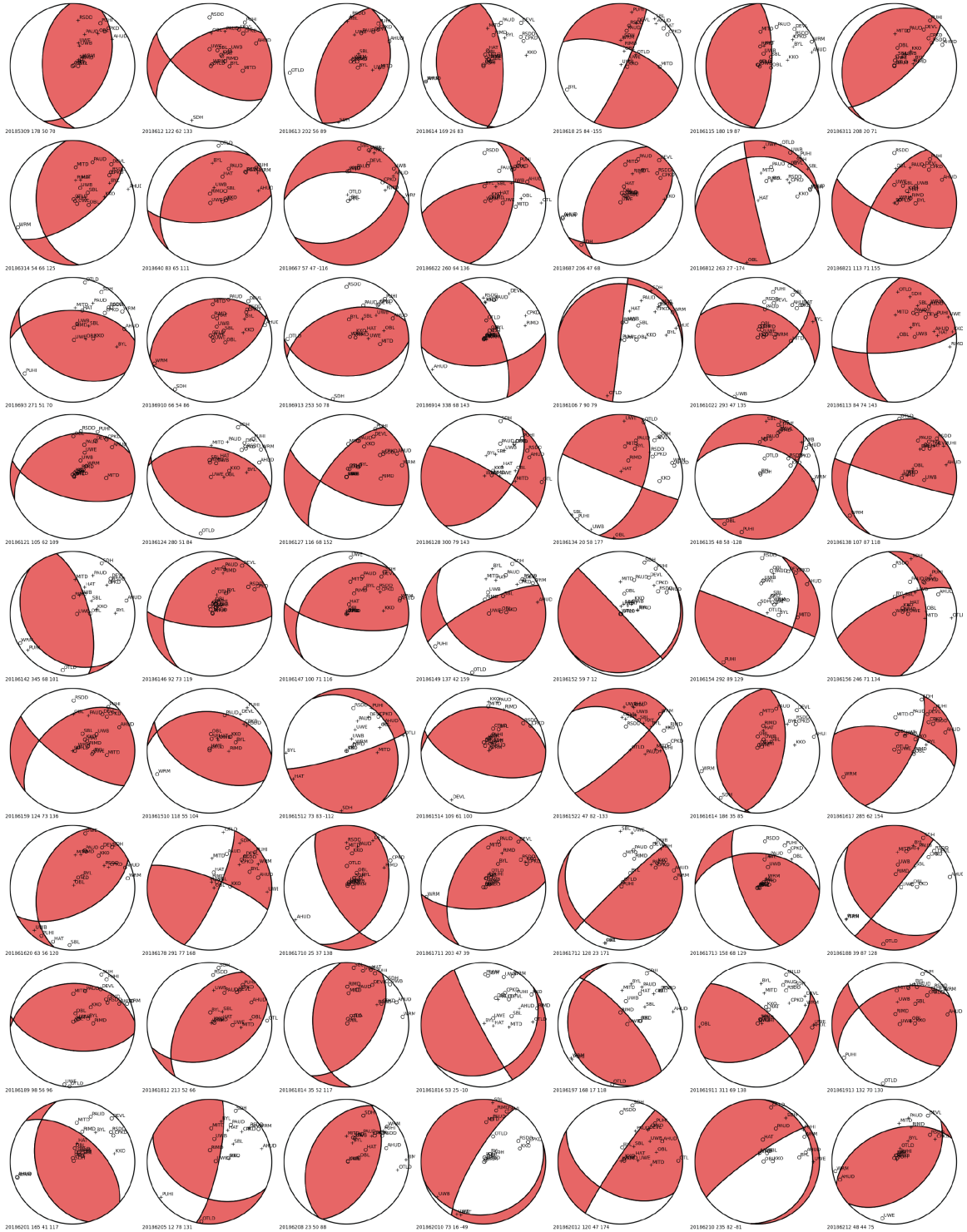
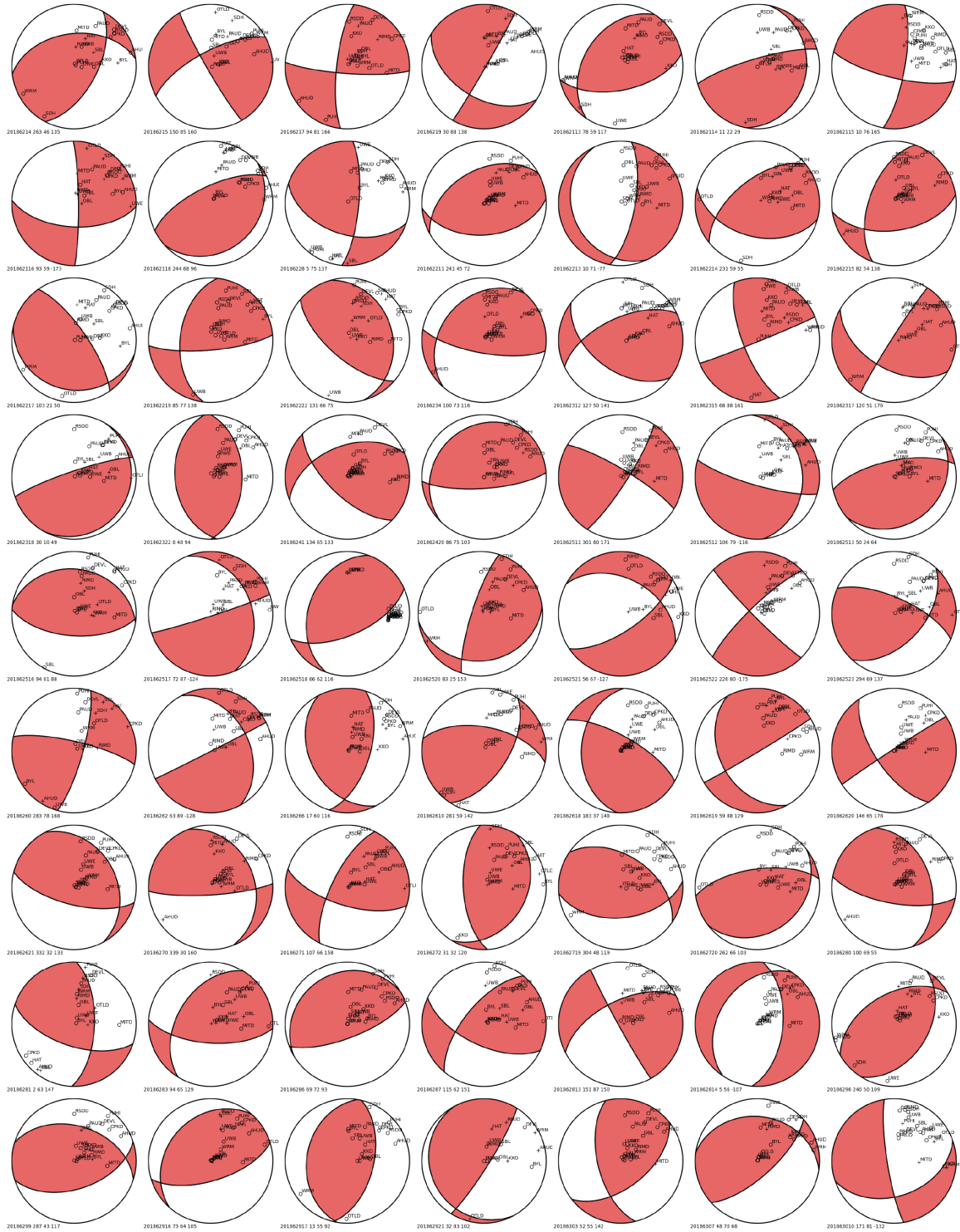
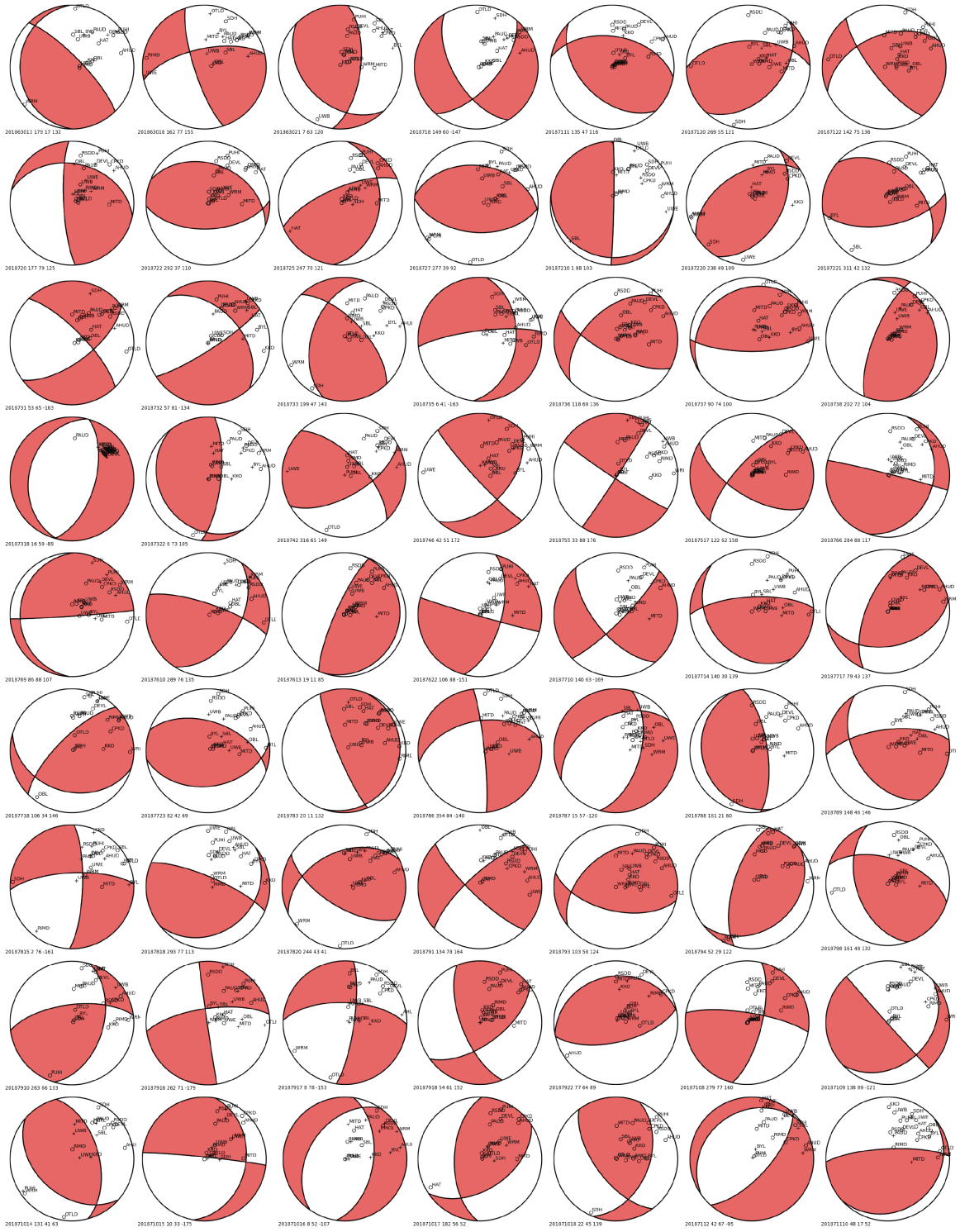


Figure A.1. Waveforms for all events within cluster 1277 recorded on station RIMD.

## A.2 Focal Mechanisms for Viable Clusters of Interest









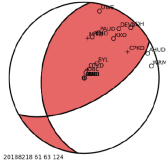
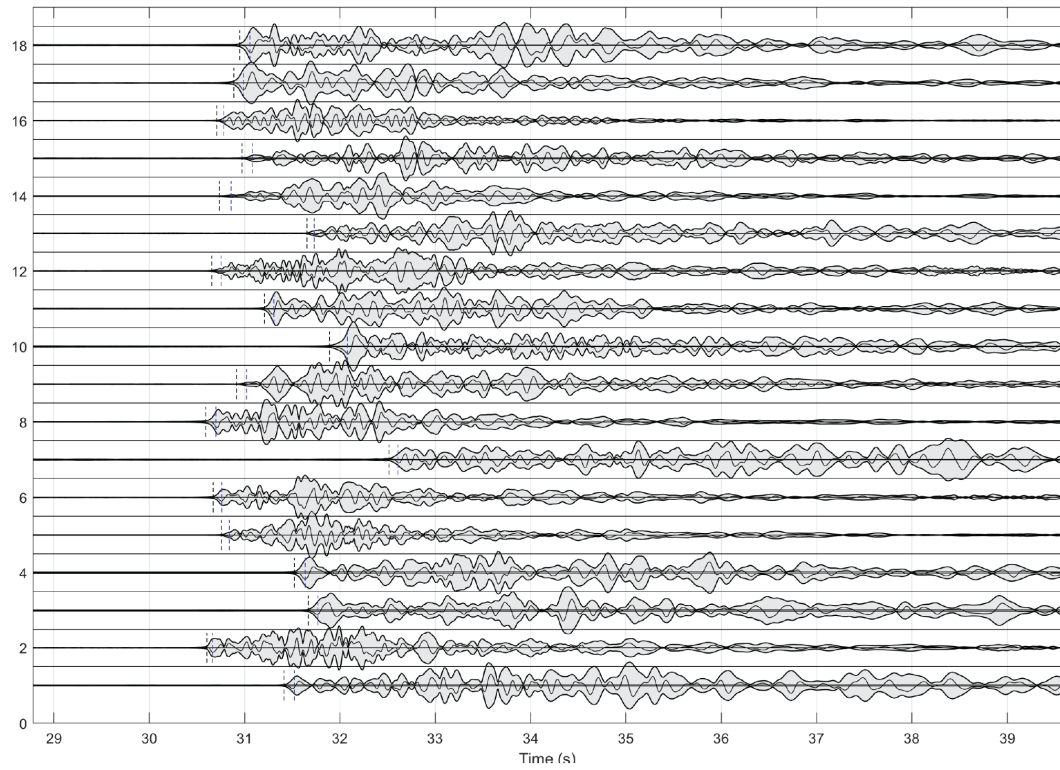


**Figure A.2.** Focal mechanism models for each cluster of interest with enough station data to send through HASH. Each mechanism depicts mismatched stations and evidence of a ring fault structure to the northeast.

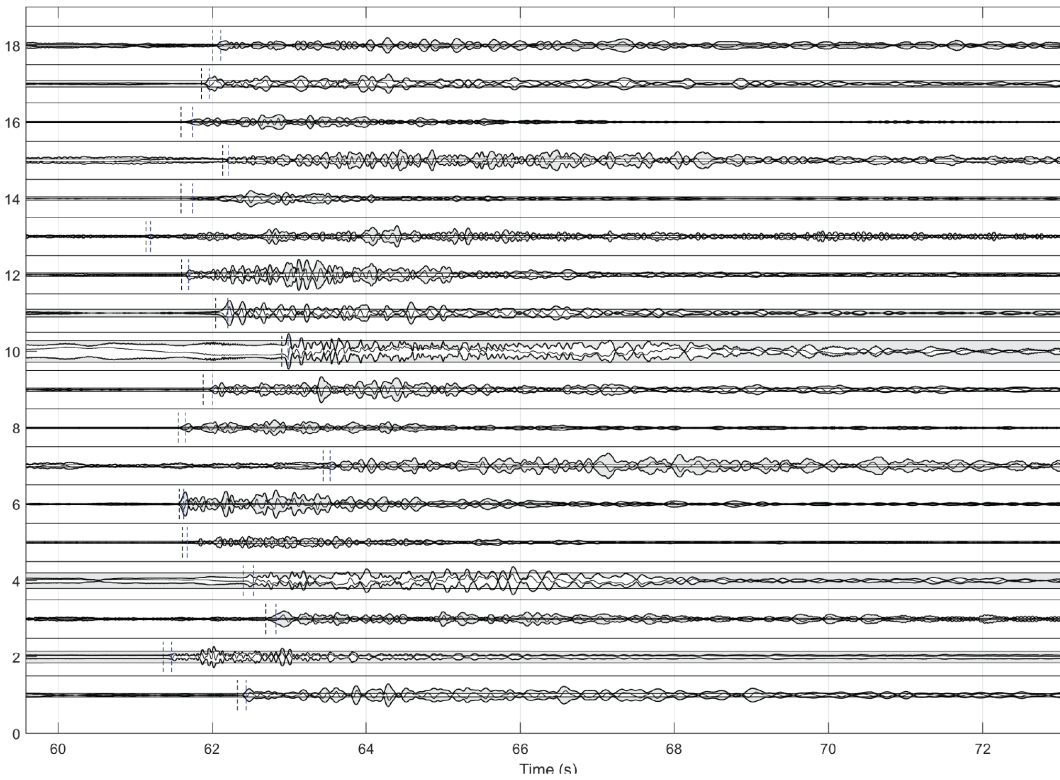


### A.3 Interactive Picking Plots for "Crack Closing" Clusters

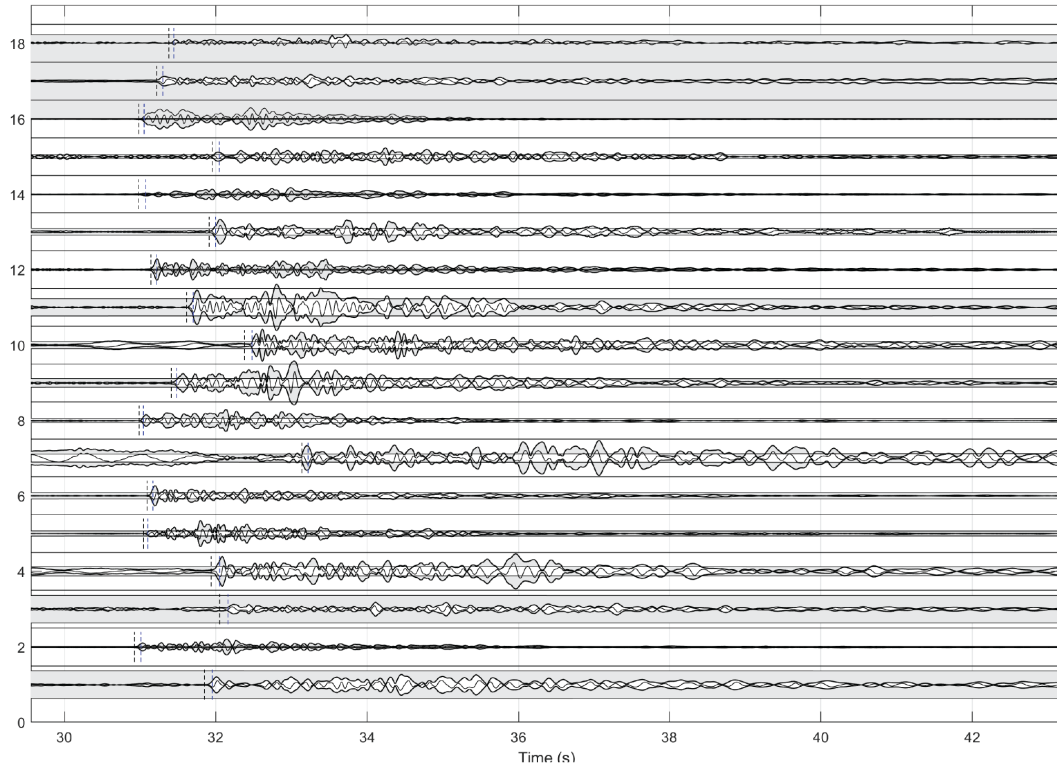
41



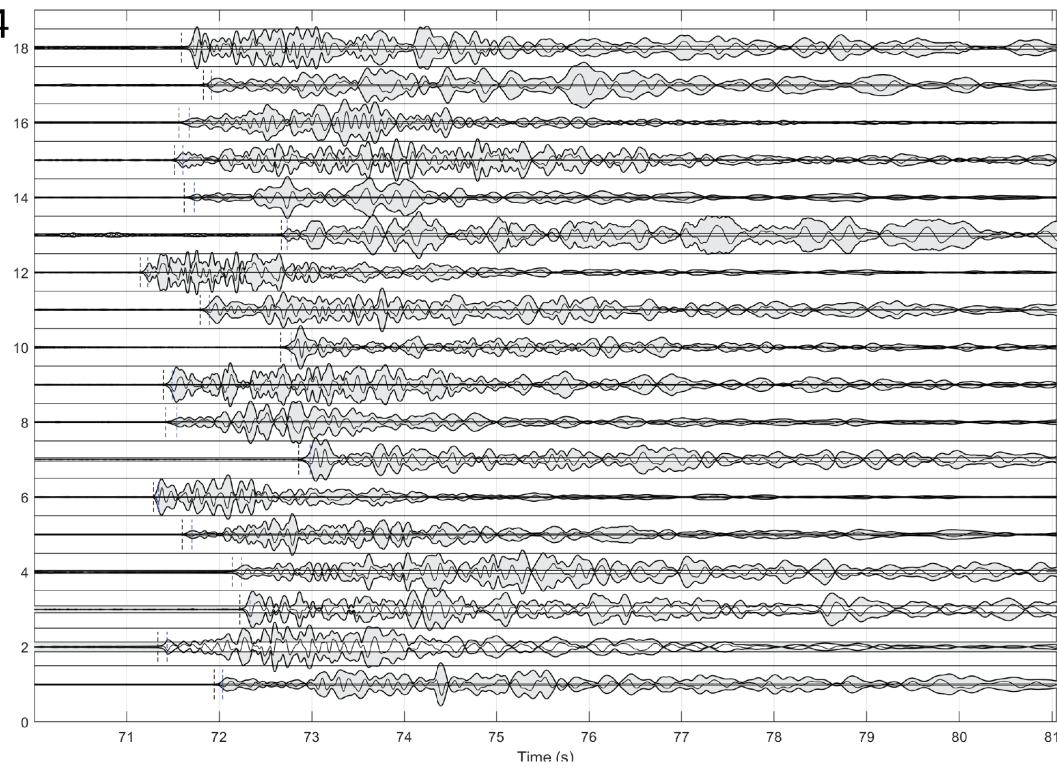
76



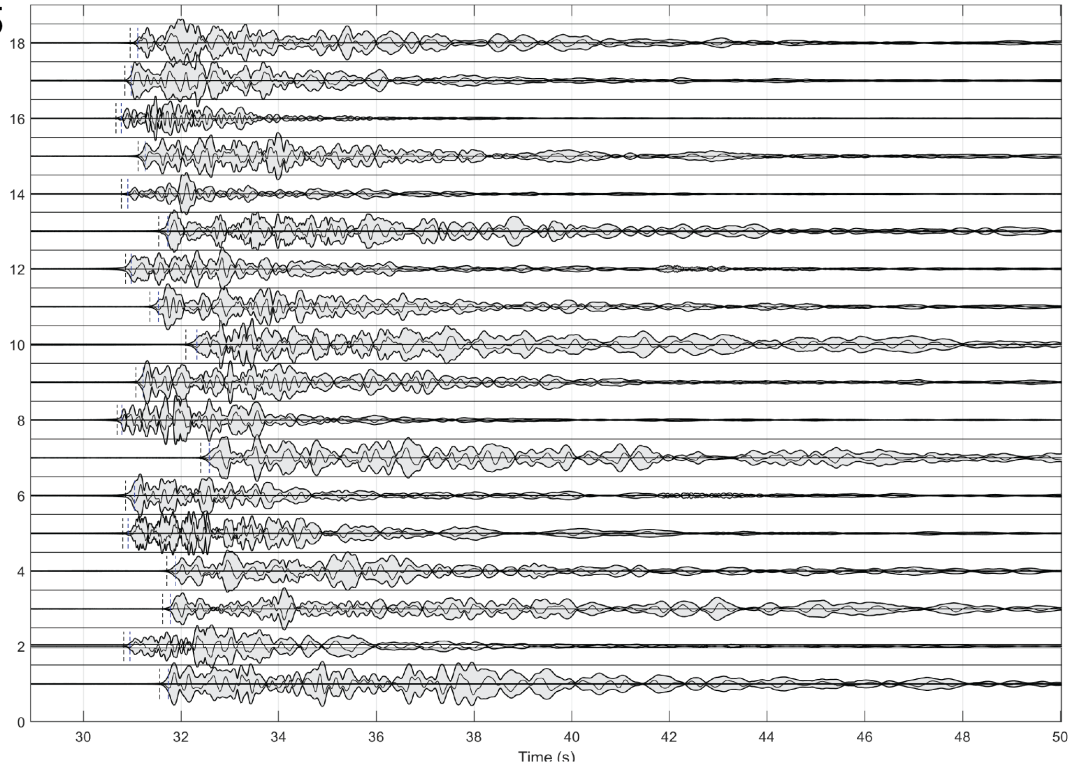
87



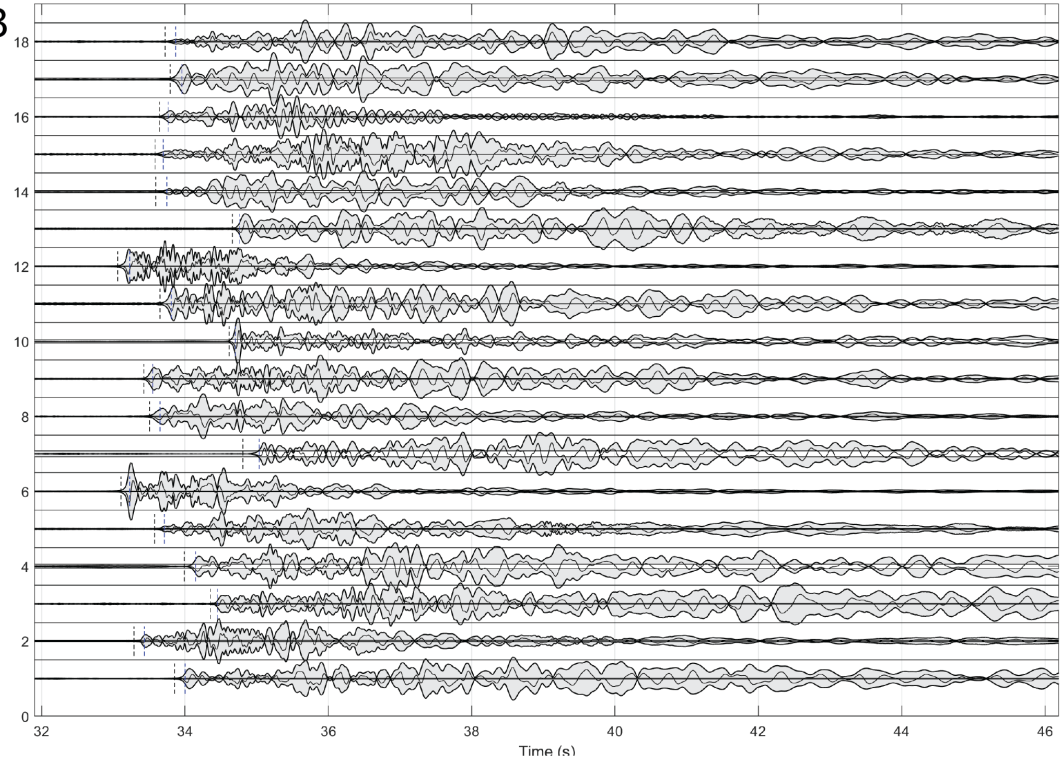
104



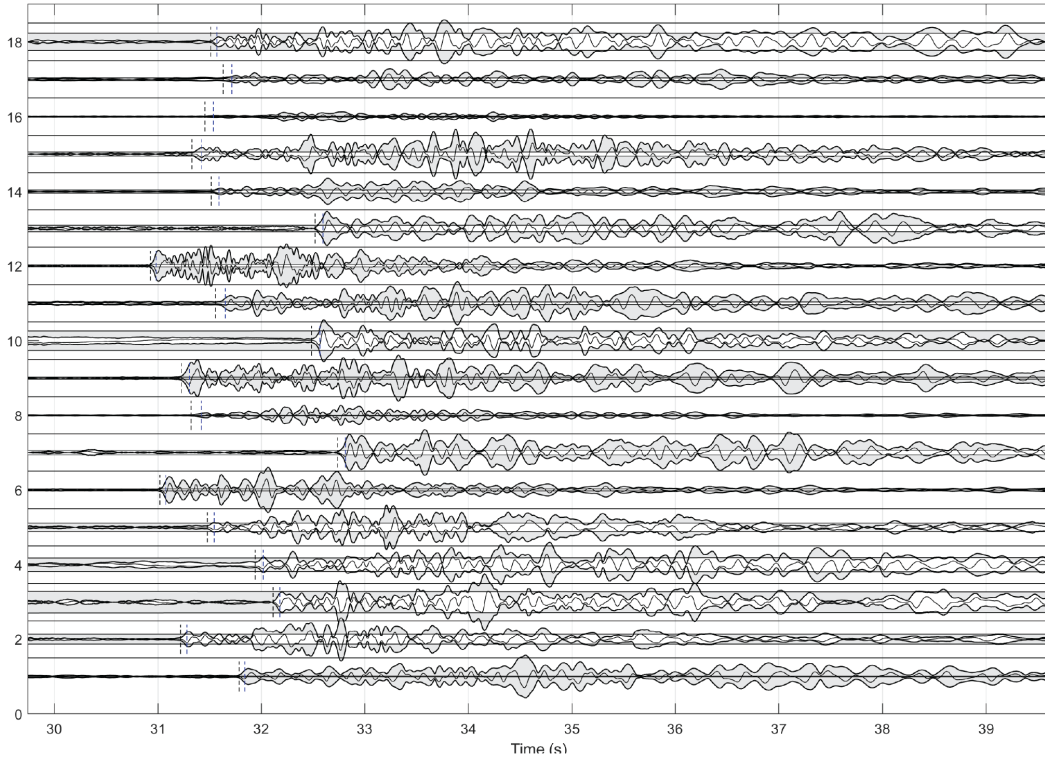
145



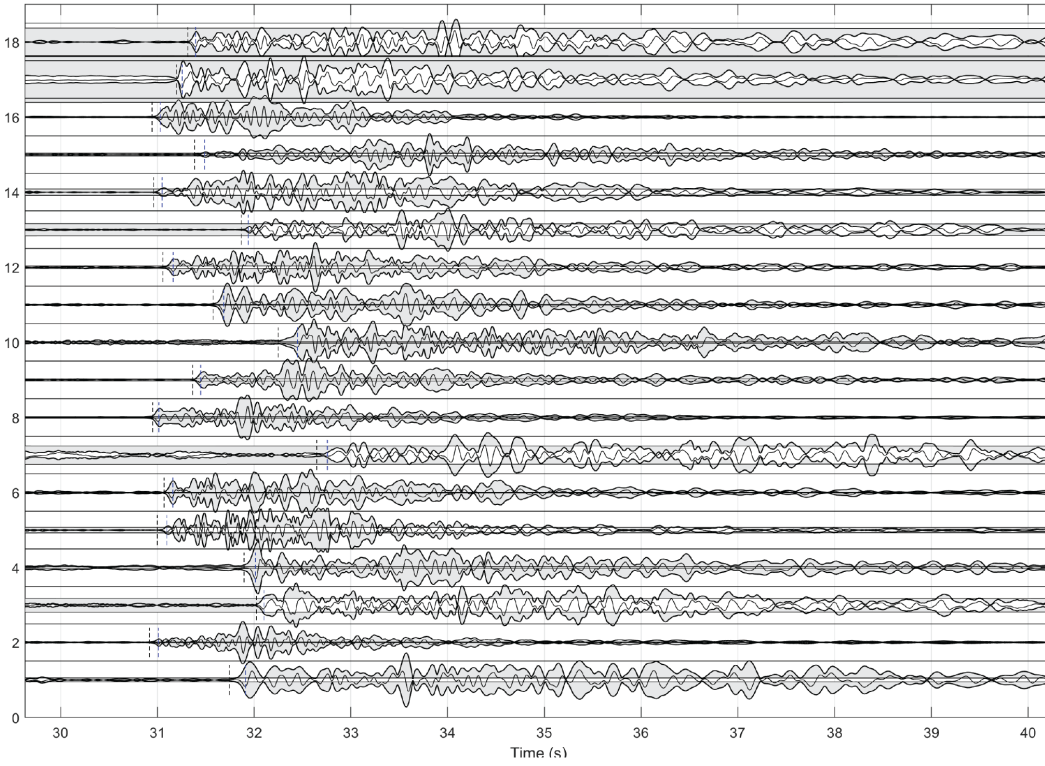
153



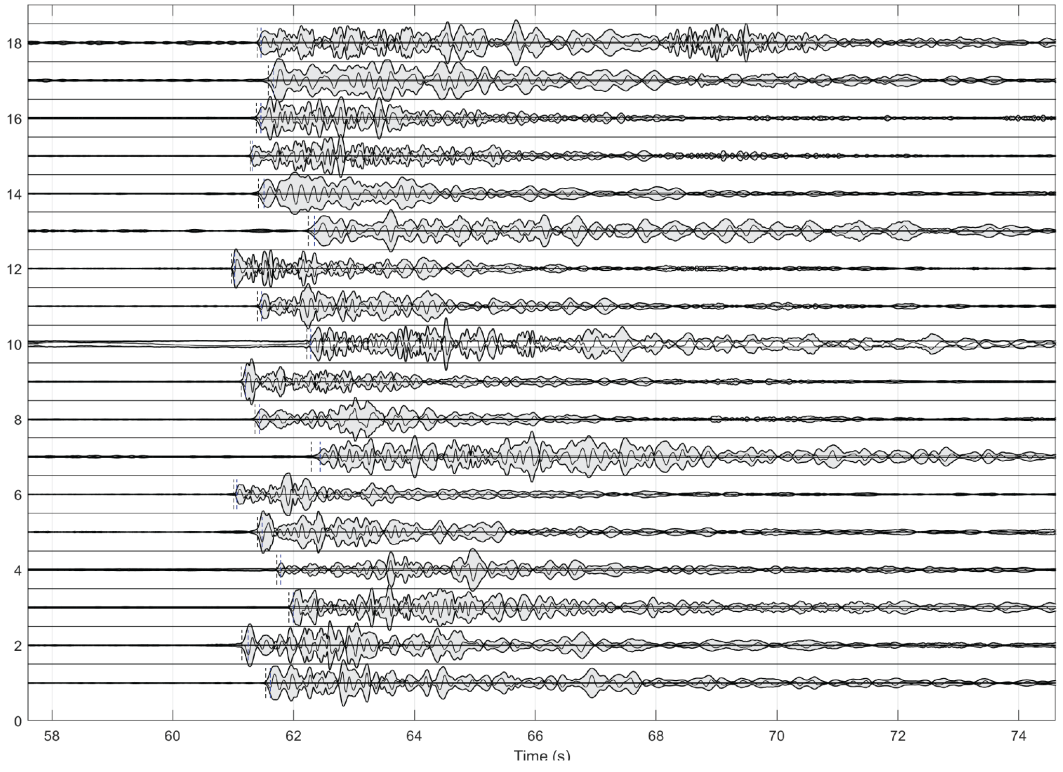
160



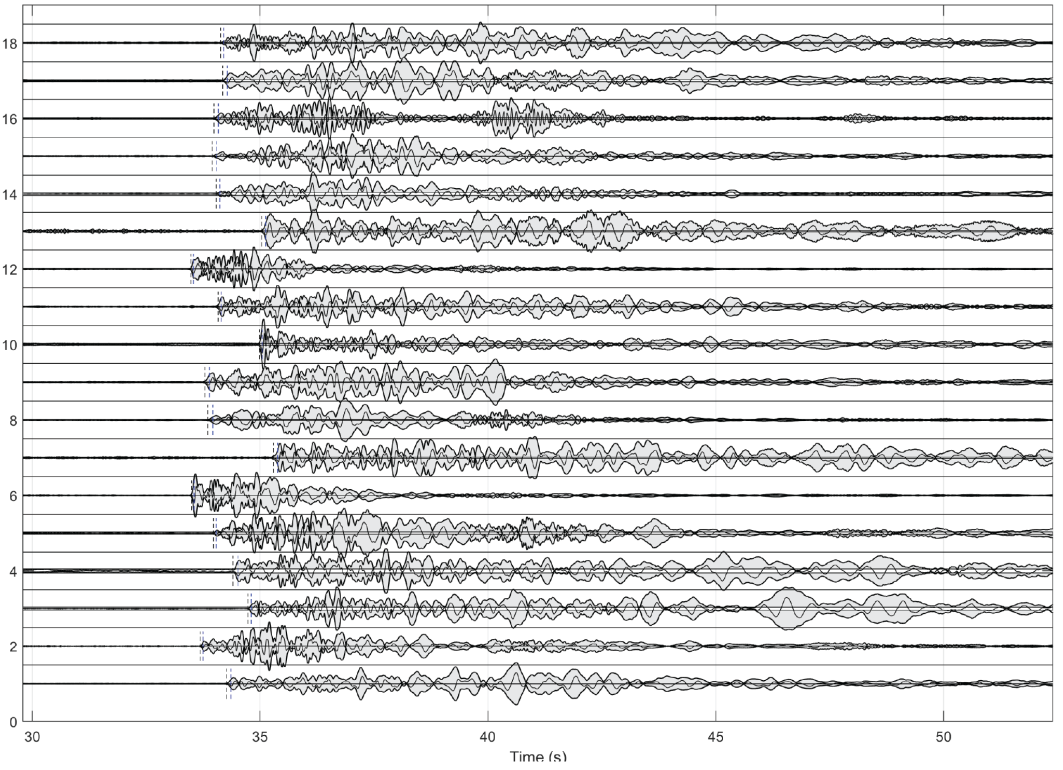
162



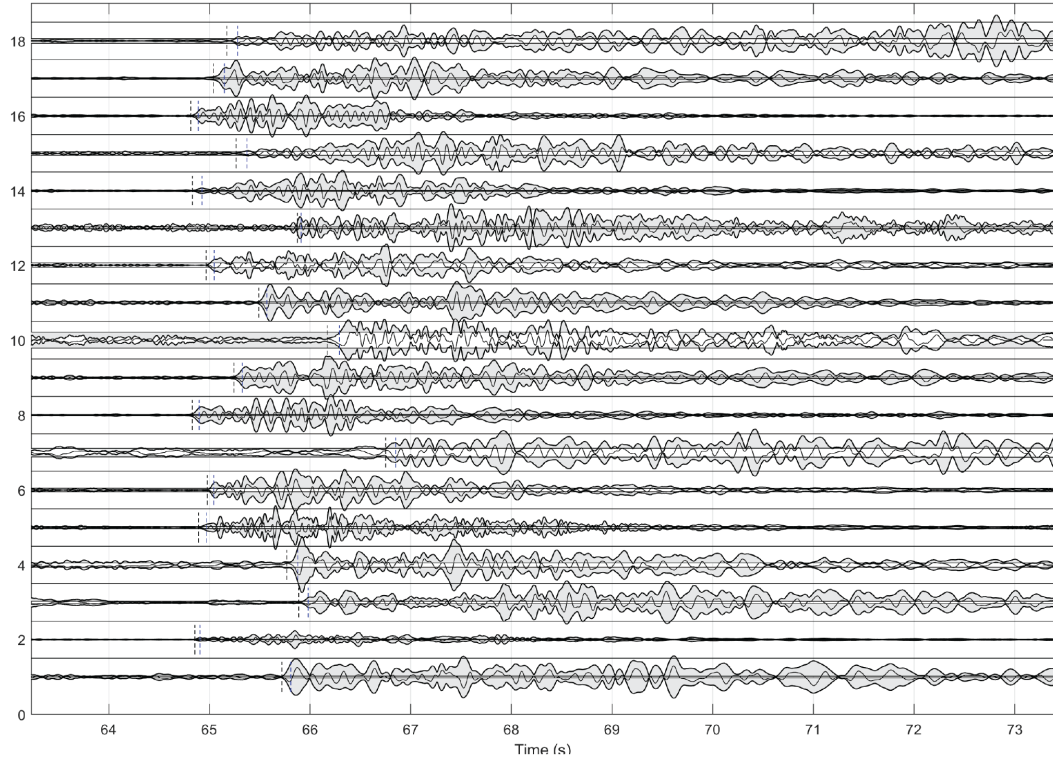
167



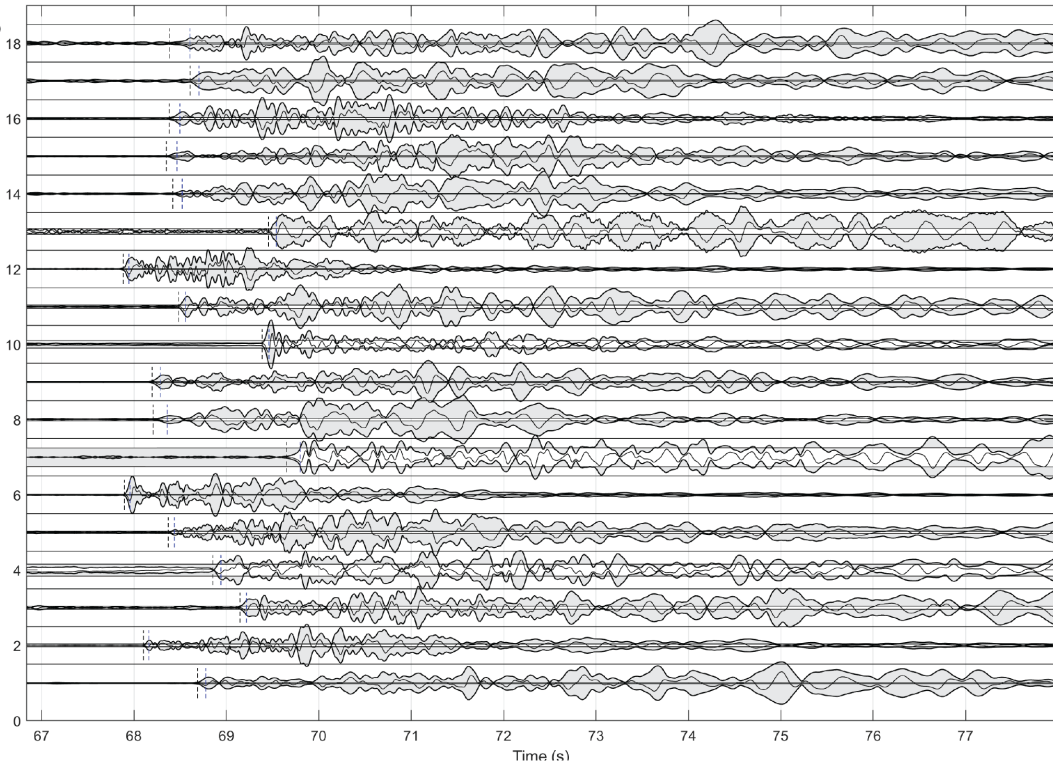
168



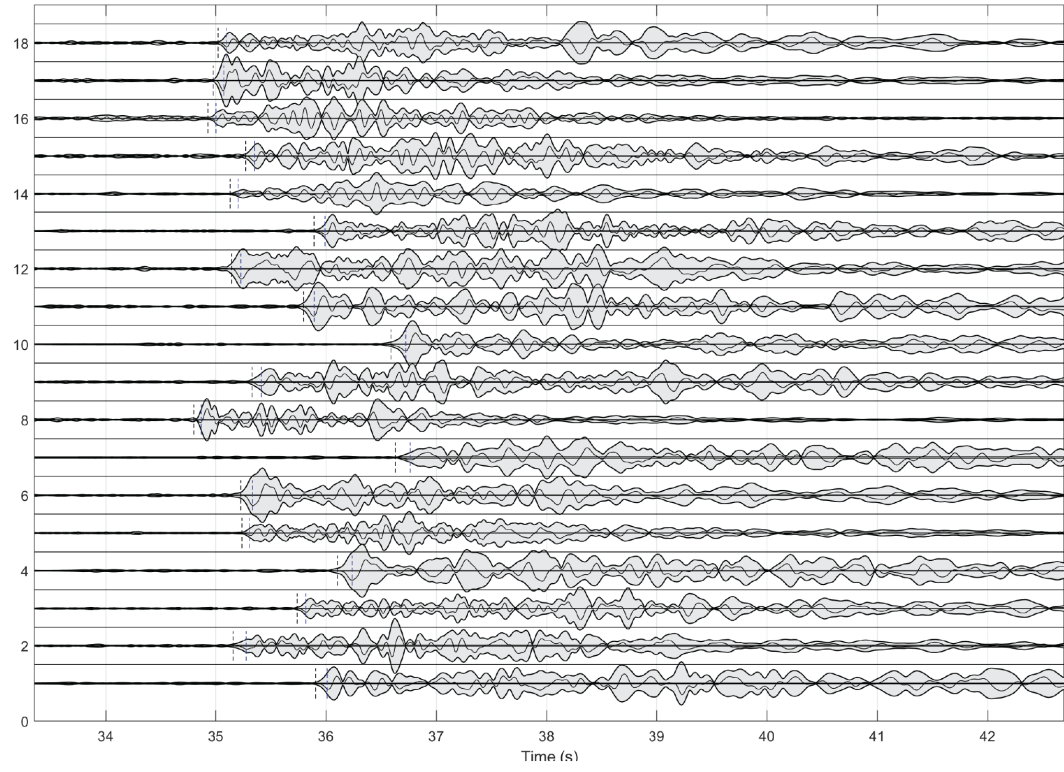
207



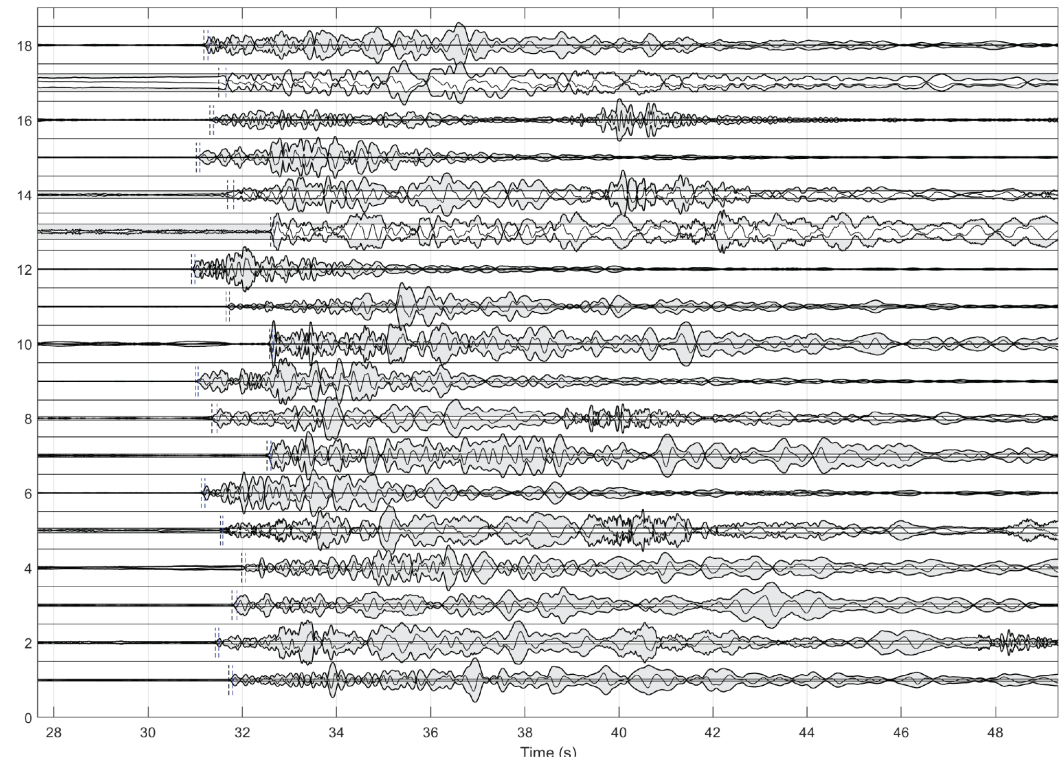
228



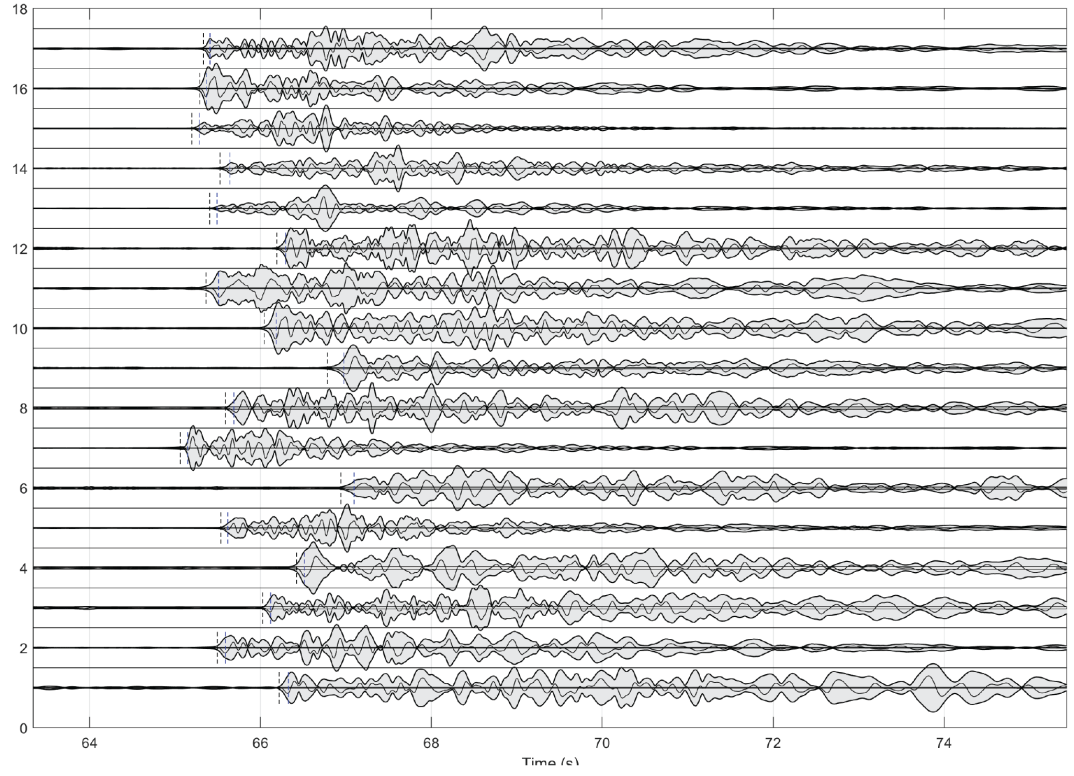
229



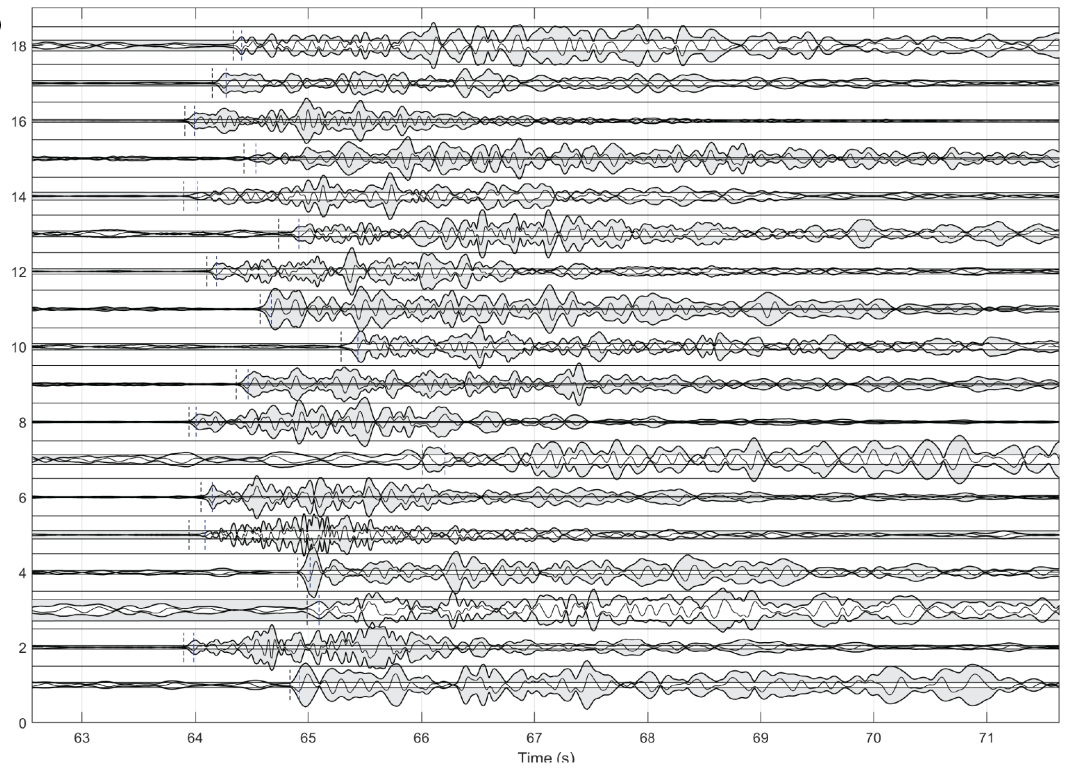
285



288

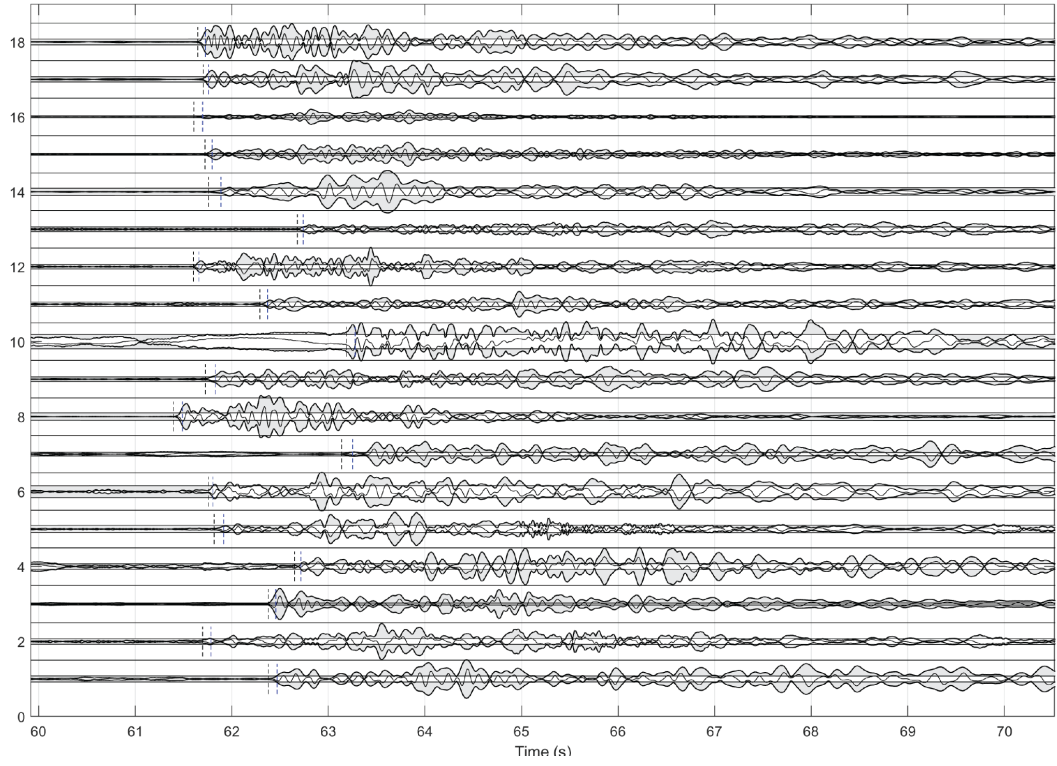


416

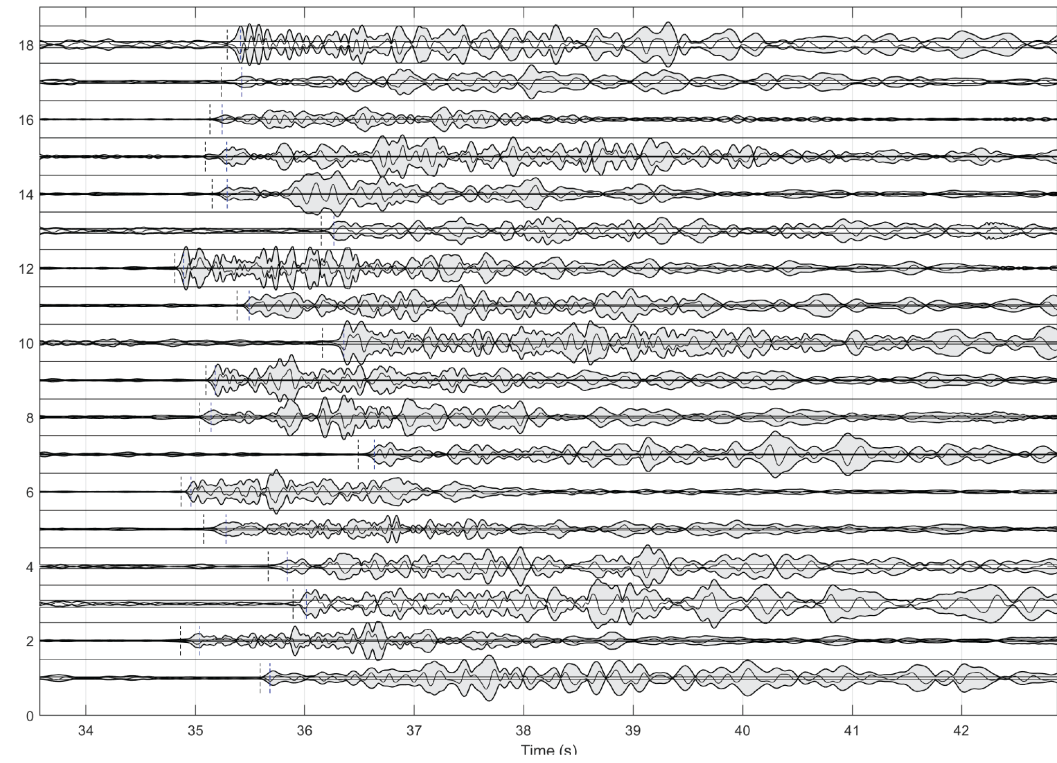




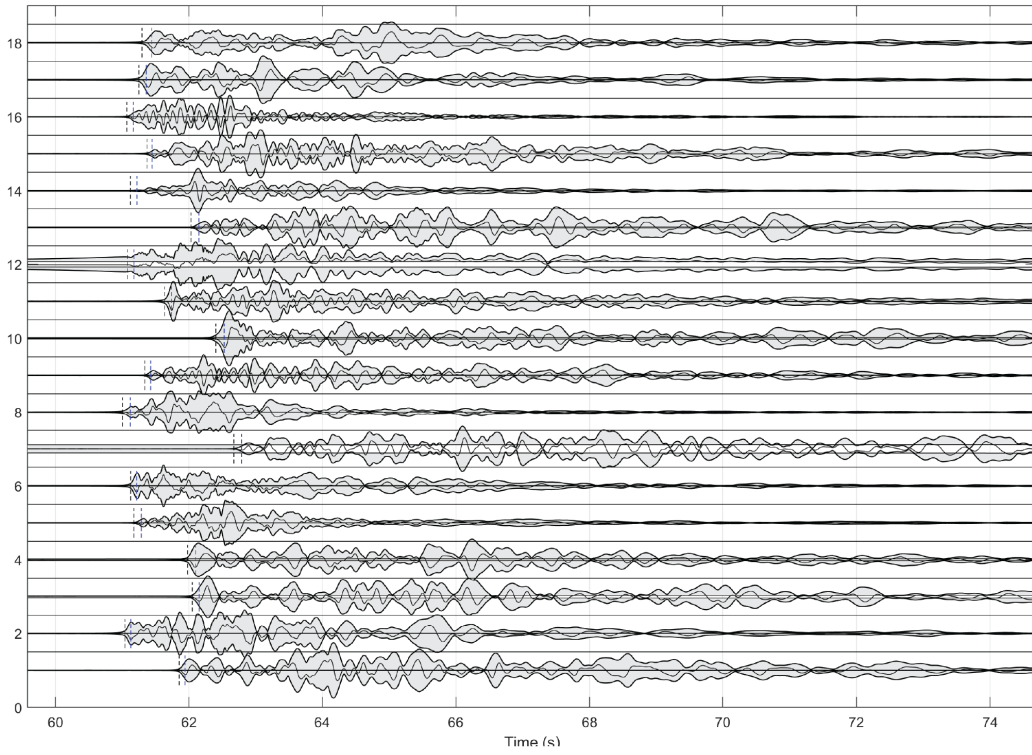
525



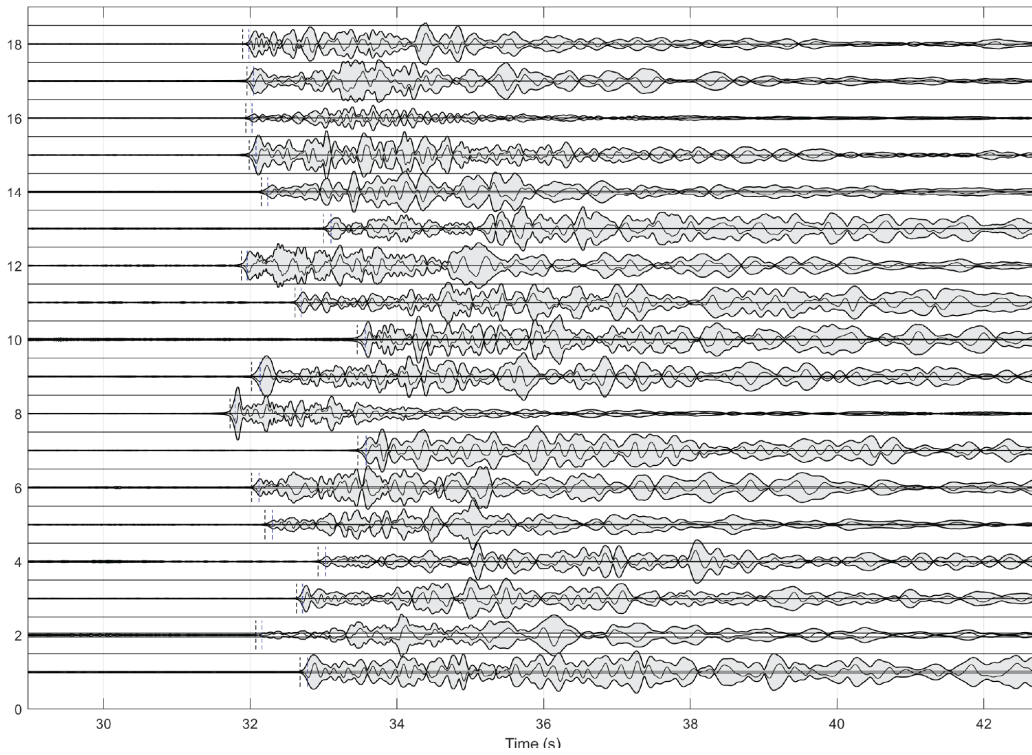
734



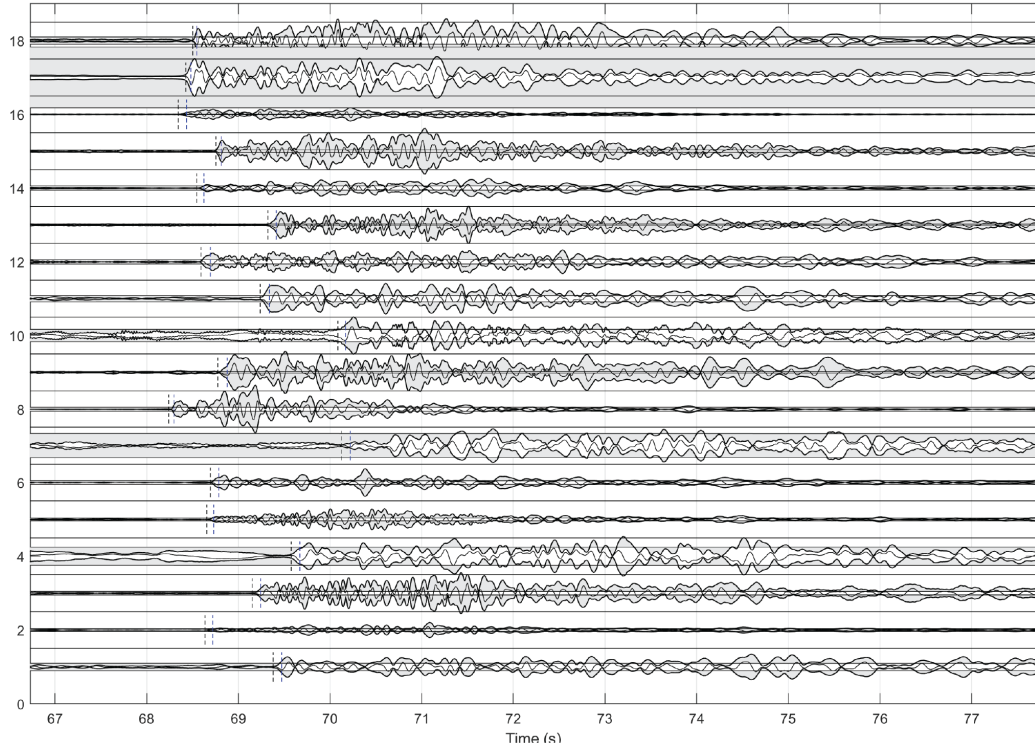
765



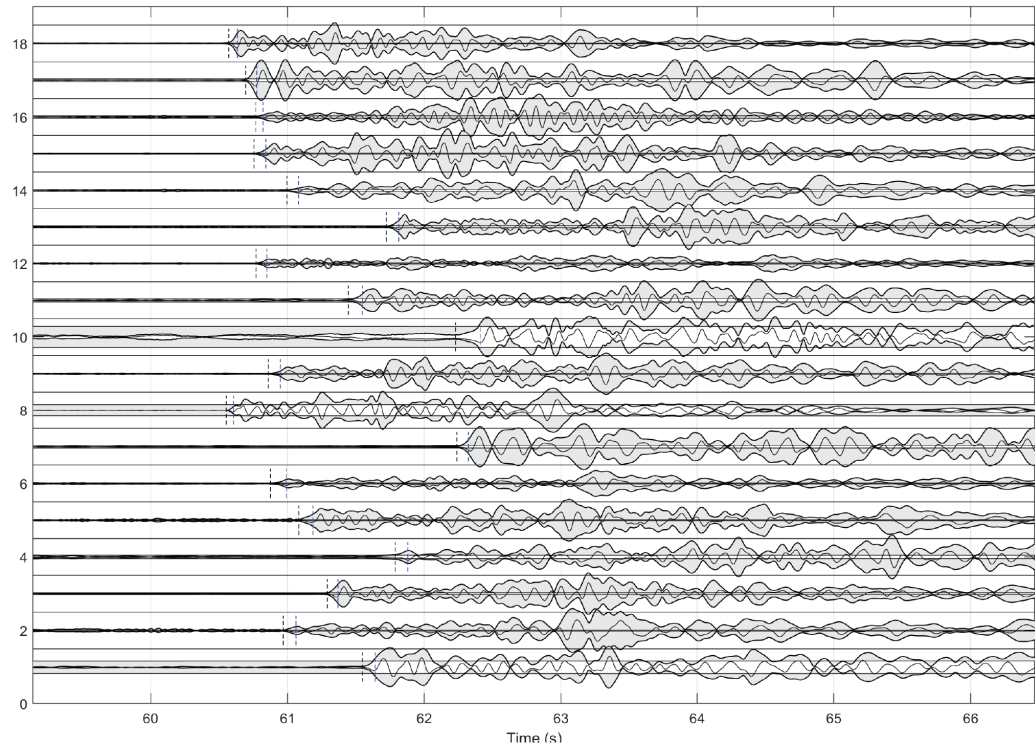
884



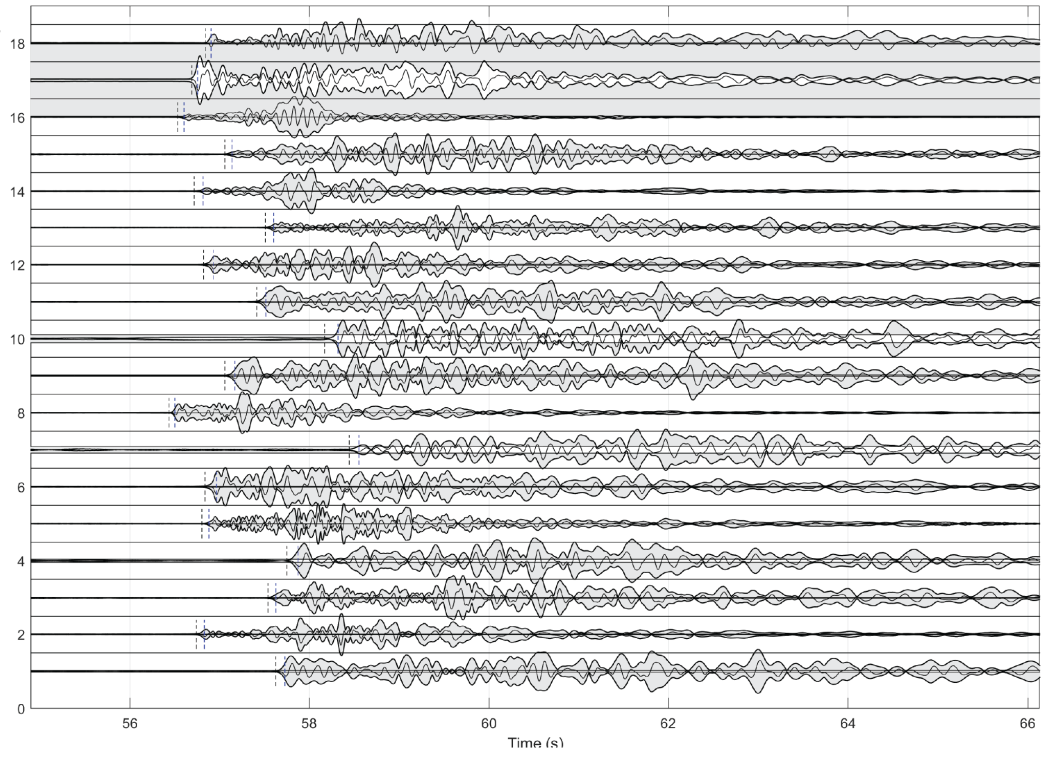
953



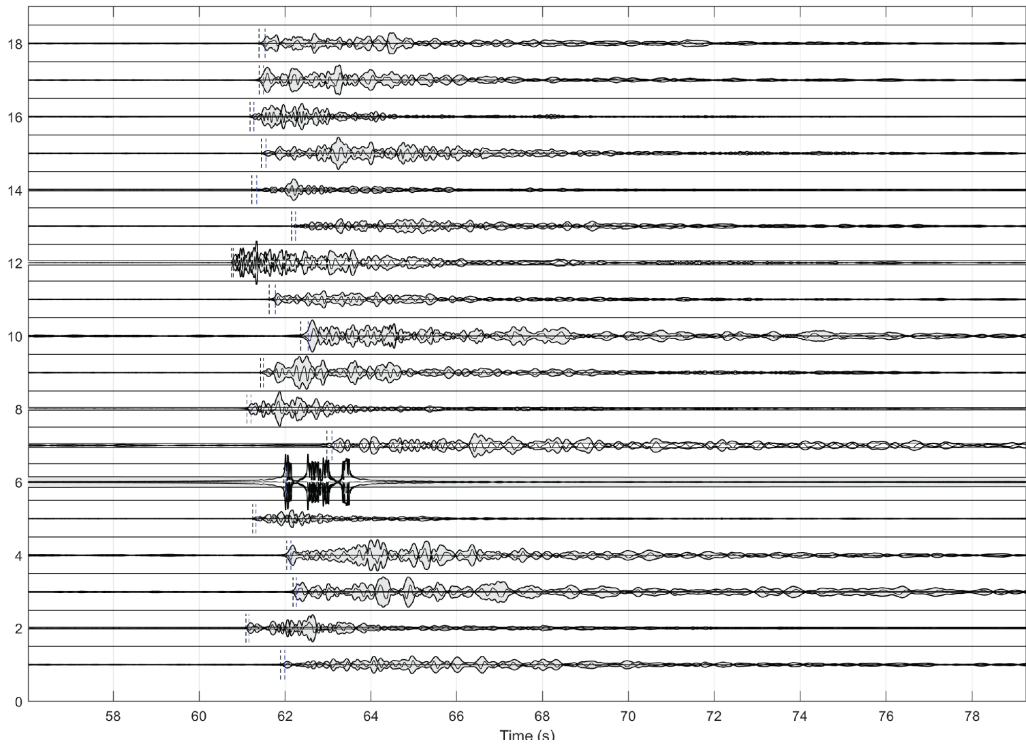
1016



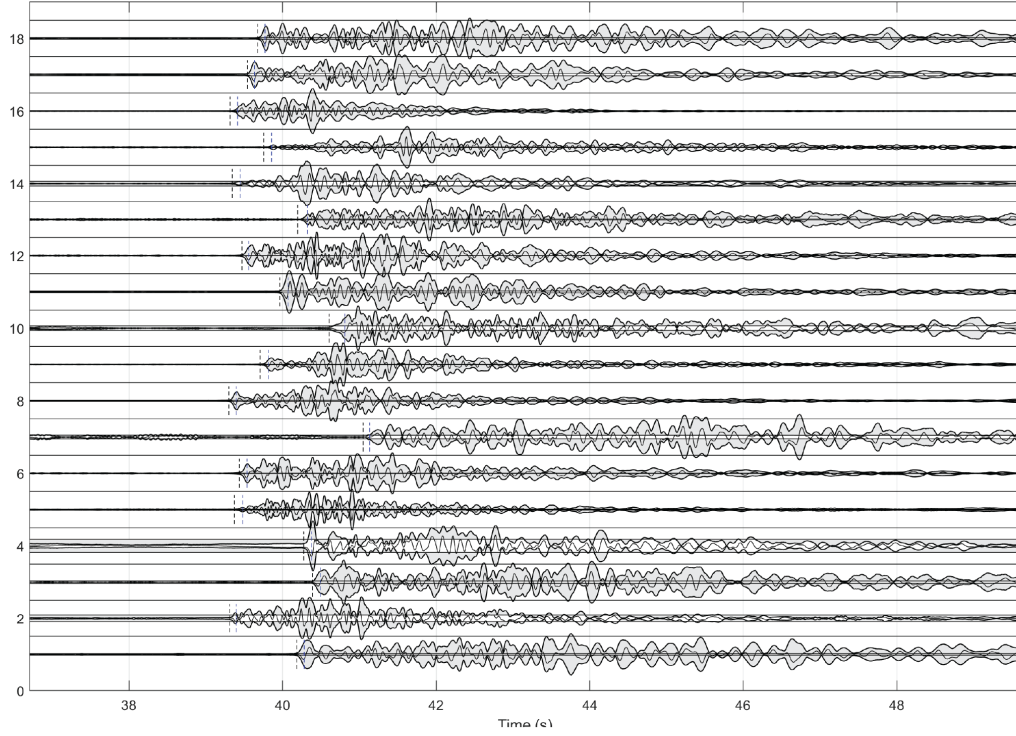
1178



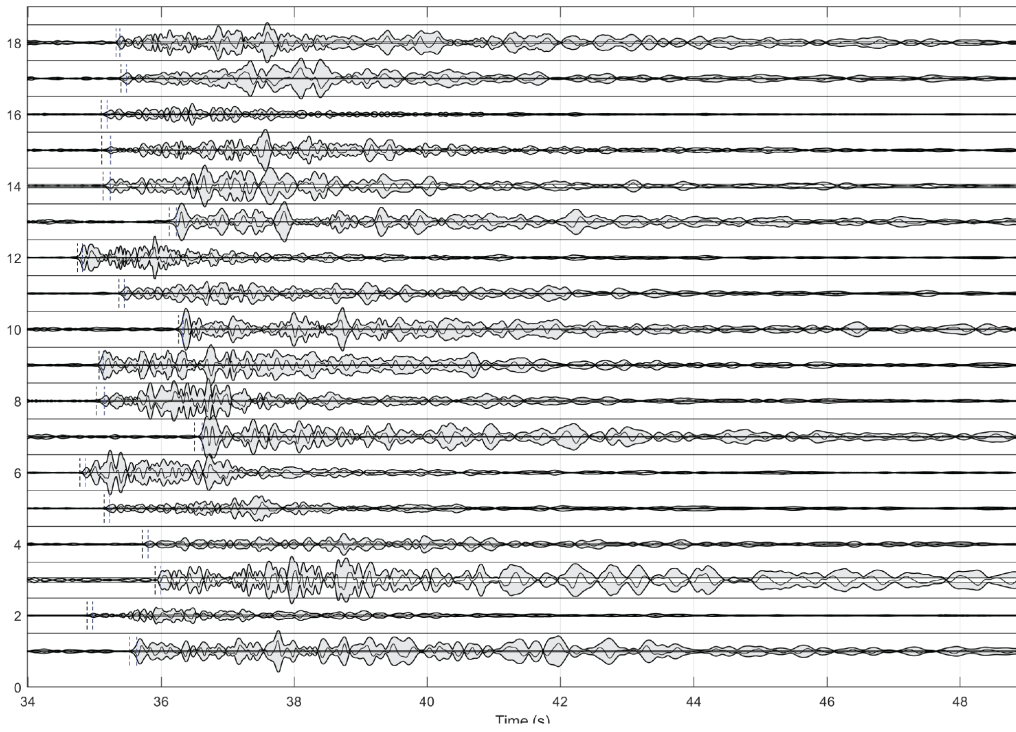
1205



1238



1277



1295

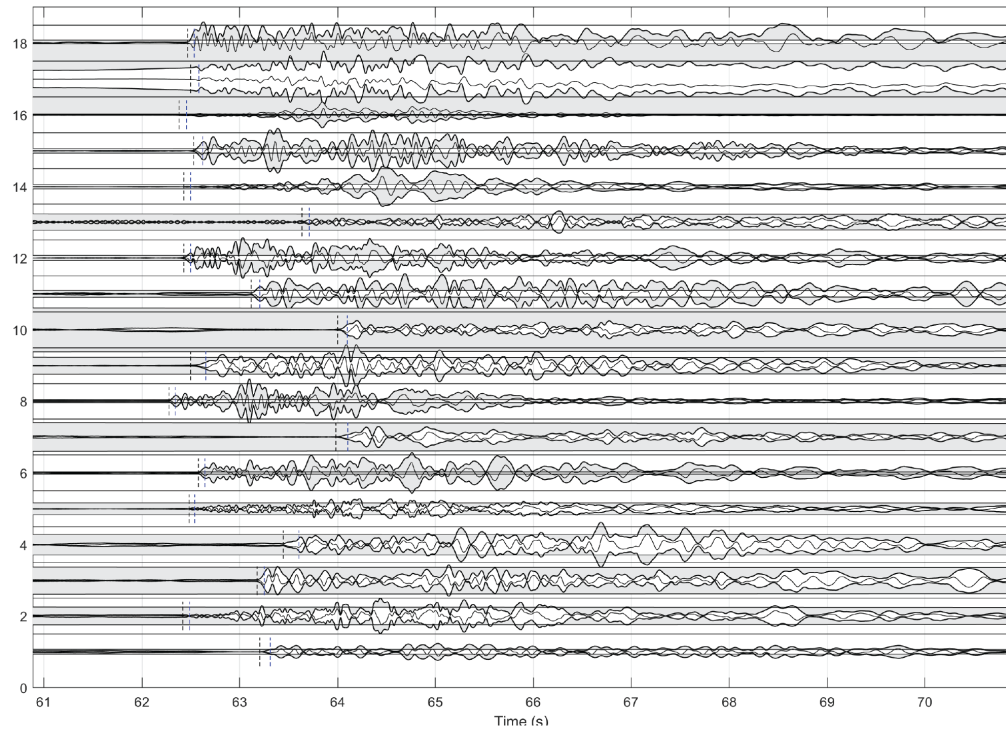


**Figure A.3.** The interactive picking plots used to pick P-wave arrivals, with arrival picks notated by dashed lines, for clusters of interest we have claimed to be “crack-closing” events. Each cluster presented here was recorded as having 100% dilatational first motions, though we determined that “crack-closing” clusters include all clusters with more than 80% dilatational first motions, leaving room for human error during the picking process.